Physics of the Earth and Planetary Interiors 363 (2025) 107348

Contents lists available at ScienceDirect

Physics of the Earth and Planetary Interiors

journal homepage: www.elsevier.com/locate/pepi

On the thermal evolution and magnetic field generation of planet Mercury

Jurrien Sebastiaan Knibbe [a,b], Attilio Rivoldini [a,*], Yue Zhao [a], Tim Van Hoolst [a,c]

[a] Royal Observatory of Belgium, Ringlaan 3, Ukkel 1180, Belgium
[b] Faculty of Sciences, Vrije Universiteit Amsterdam, De Boelelaan 1085, Amsterdam 1081 HV, the Netherlands
[c] Institute of Astronomy, KU Leuven, Celestijnenlaan 200D, Leuven 3001, Belgium

ARTICLE INFO

Keywords:
Mercury
Thermal evolution
Magnetic field
Core

ABSTRACT

Heat transfer through convection in Mercury's large core may be limited to a liquid layer between a solid inner core and a stably stratified outer liquid layer. Convection in the thin mantle may even have entirely stopped. Here, we consider the transition from convective to conductive heat transport in a coupled thermal evolution model of the mantle and core and assess implications for the generation of the magnetic field.

We argue that a conductive temperature profile best describes the temperature in regions of the core with a subadiabatic heat flux. Implementing an adiabat in these regions in a model of the evolution of the core, as is often done, implicitly assumes the existence of a mechanism that transports heat downward. Such a mechanism not only consumes power that could otherwise be available for sustaining dynamo action, but is also unlikely to be effective.

We show that a thermally convective layer deep in Mercury's liquid core below a thermally stratified layer is more likely to persist until present if light elements depress the liquidus of the core by several hundred degree compared to iron. Substantial partitioning of light elements into the liquid core can drive strong compositional convection in the upper part of Mercury's core, but this may not be in line with dynamo studies that are consistent with the observed magnetic field. Therefore, thermal evolution scenarios with light elements in the core that depress the core liquidus significantly but do not strongly fractionate into the core liquid are the most consistent with the present-day core dynamo.

Present-day dynamo action below a thermally stratified layer does not necessarily imply that the mantle is currently convective. If the mantle has a high concentration of radiogenic elements and a low viscosity, it must be convecting, but mantle convection can have ended before the present for a more viscous mantle with low concentration of radiogenic elements.

1. Introduction

Mercury has a weak and highly axisymmetric dipole magnetic field, which is offset to the north due to its high quadrupole-dipole ratio (Anderson et al., 2012; Thébault et al., 2018; Wardinski et al., 2019; Wardinski et al., 2021; Genova et al., 2021). Core convection in this slowly rotating planet (Mercury's rotational period is 58 Earth days) is expected to produce a magnetic field dominated by small-scale structures that vary rapidly with time and are stronger than the observed field (Christensen, 2006). This difference cannot be explained solely by the geometric decay of the magnetic field propagating from the core to an orbiting spacecraft. In our current understanding of Mercury's weak and broad-scale magnetic field, dynamo action likely takes place deep in the liquid core whereas the upper part of the liquid core is a stably stratified layer that attenuates the small-scale rapidly-varying components of the magnetic field by the skin effect (Christensen, 2006). Additionally, zonal thermal winds are generated that convert part of the poloidal field to a toroidal field in the stably stratified layer by the ω-effect, thereby rendering the observable magnetic field strongly axisymmetric (Christensen and Wicht, 2008). Thermal evolution studies predict that the heat flux at the core-mantle boundary (CMB) dropped below the adiabatic heat flux before the present day and thermally stratified the outer part of the core (e.g. Stevenson et al., 1983; Knibbe and van Westrenen, 2018). The influence of compositional buoyancy, for example generated by light elements partitioning into the liquid core upon inner core solidification, on the dynamics and dynamo of the core is less understood. Manglik et al. (2010) and Takahashi et al. (2019) performed core dynamo simulations of a core with compositional

---

* Corresponding author at: Royal Observatory of Belgium, Ringlaan 3, Ukkel 1180, Belgium.
E-mail addresses: jsknibbe@hotmail.com (J.S. Knibbe), attilio.rivoldini@oma.be (A. Rivoldini).

https://doi.org/10.1016/j.pepi.2025.107348
Received 15 April 2024; Received in revised form 20 March 2025; Accepted 21 March 2025

convection and a thermally stratified upper layer. The simulations by Manglik et al. (2010) show the formation of plumes at the inner core boundary that are mainly driven compositionally but also thermally and can propagate into the thermally stratified layer. This contributes to the magnetic field and causes the simulated magnetic field to be stronger than the observed field. In the simulations of Takahashi et al. (2019) that reproduce the main characteristics of the observed magnetic field of Mercury, in particular the observed ratio of the dipole and quadrupole, the light elements released at the inner core boundary are not able to enter the thermally stable layer. As a consequence, the fluid core below the stable layer will become less dense and it is expected that this process will ultimately lead to an unstable situation with a light convecting layer below a heavier stable layer. In this paper, we aim at modelling the long-term evolution of Mercury in a consistent way, and we will assume that light elements enter the thermally stable layer and assume it occurs in the form of fingering convection (Guervilly, 2022). We nevertheless caution the reader that the effect of fingering convection on dynamo action is largely unknown and has not been investigated in simulations for realistic Mercury core models. Both of the simulation studies mentioned above show that the characteristics of Mercury's magnetic field are very sensitive to the fluxes of heat and light elements through the liquid core.

The transport of heat and light elements in Mercury's core is related to the long-term thermochemical evolution of the entire planet. In particular, the heat flux through the CMB needs to be sufficiently high to meet necessary conditions for dynamo action (e.g. Lister and Buffett, 1995; Gubbins et al., 2004; Nimmo, 2007; Labrosse, 2015). According to Williams et al. (2007), a sufficiently high present-day CMB heat flux for dynamo action can only be achieved if Mercury's mantle is convective at present day. However, Guerrero et al. (2021) suggest that the CMB heat flux increases when mantle convection ends due to the thermal relaxation of conduction in the mantle. They then argue that dynamo generation may be possible if the mantle is not convective. Additionally, the transport of light elements through the liquid core depends, among others, on the cooling rate of the core and on the solid/liquid partitioning behaviour of the light elements. The partitioning strongly depends on the composition of the core. For example, in iron-rich binaries sulfur (S) partitions almost exclusively into the liquid (e.g. Fei et al., 1997, 2000), carbon (C) partitions at approximately a 3 to 1 ratio between liquid and solid (Fei and Brosh, 2014), and Si partitions almost equally between liquid and solid (e.g. Morard et al., 2014).

This study aims to assess which thermal evolution scenarios of Mercury yield a buoyancy forcing in the core at present that is consistent with the observed magnetic field. Due to the large mass ratio of the metallic core over the silicate mantle, several aspects of thermal evolution modelling of both the mantle and core require specific attention. Firstly, unlike Earth's mantle, convection in Mercury's thin silicate mantle may have ended during its evolution (Schubert et al., 1979; Michel et al., 2013; Tosi et al., 2013a; Thiriet et al., 2019; Guerrero et al., 2021) because convection is more difficult to maintain in a thin shell (Schubert et al., 2001). Many studies modelling parameterized thermal evolution limit their investigation to the time period when the mantle is convective (Schubert et al., 1979; Thiriet et al., 2019). In other such studies, when convection in the mantle ends, heat transport in the mantle switches instantaneously to conduction (Hauck et al., 2004; Grott et al., 2011; Tosi et al., 2013a), leading to a discontinuous CMB heat flux (see Hauck et al., 2004), which affects the evolution of the core. Some models limit their investigation to the time period when the mantle is convective (Schubert et al., 1979; Thiriet et al., 2019). Other models change the modelling of heat transport in the mantle instantaneously from convective to conductive when convection ends (Hauck et al., 2004; Grott et al., 2011; Tosi et al., 2013a). This introduces a discontinuity in the CMB heat flux (see Hauck et al., 2004), which affects the evolution of the core, though in some studies the discontinuity is small (Tosi et al., 2013a). Unlike parameterised thermal evolution, numerical mantle convection simulations show a smooth transition to a conductive state (e.g. Guerrero et al., 2021). To our knowledge, parameterised thermal evolution models of the mantle that smoothly transition from a convective state to a conductive state are not available.

Secondly, thermal evolution models usually describe the temperature profile of the core by an adiabat, based on the assumption that the heat flux through the core is superadiabatic and generates convection. It is usually not taken into account that heat transport can be subadiabatic in large regions of Mercury's core (we refer to a region with subadiabatic heat flux as 'thermally stratified'). Although it has not explicitly been mentioned in our previous thermal evolution studies (Knibbe and van Westrenen, 2018; Knibbe and Van Hoolst, 2021), which included a thermally stratified layer in the upper core, also the inner core is thermally stratified (see also Sec.[2.3]). Thermally stratified regions in a metallic core are not specific to Mercury – Earth's inner core (Buffett, 2012; Labrosse, 2014), possibly a thin upper layer in Earth's outer liquid core (Labrosse et al., 1997; Buffet, 2014; Greenwood et al., 2021a), the Moon's core (Konrad and Spohn, 1997), and the core of Mars (Greenwood et al., 2021b) are likely thermally stratified – but specific for Mercury is that its large core is the dominant energy reservoir of the planet. Therefore, the specifics of heat transport through the core can significantly affect the thermal evolution of the entire planet (Knibbe and Van Hoolst, 2021) and with it the geometry and strength of its magnetic field (Christensen, 2006; Christensen and Wicht, 2008).

The assumption of an adiabatic temperature profile in a thermally stratified region implies that conductive heat transport along the thermal gradient exceeds the gross radial flux of heat. Under this assumption, a mechanism must exist that transports heat downward to make up for the difference (Loper, 1978). The downward convective heat flux associated with compositional convection in a thermally stratified layer is such a mechanism. However, that downward heat transport is likely not sufficient to maintain an adiabatic temperature profile in Mercury's core. First, compositional convection is absent in the thermally stratified inner core, unless the partitioning of light elements into the solid strongly decreases as the core cools (e.g. Gubbins et al., 2013; Labrosse, 2014). Second, in fingering convection in a thermally stratified region of the liquid core, temperature is the rapidly diffusive stable component and composition the slowly diffusive unstable component (Manglik et al., 2010; Guervilly, 2022). Therefore, sinking and rising parcels of material rapidly thermally equilibrate with their surroundings by the more efficient conduction of heat (Stern, 1960). This leads to efficient upward convective transport of light elements and less efficient downward convective transport of heat. Particularly in metallic liquids such as in an iron-rich liquid core, the heat transport by fingering convection is expected to be inefficient because the Prandtl number (the ratio of momentum diffusivity to thermal diffusivity) of liquid metal is small (Schmitt, 1983; Kunze, 2003; Radko, 2013; Garaud, 2018, 2020). As a result, the mean temperature profile in the thermally stratified layer can to a very good approximation be described by the subadiabatic conductive temperature profile (see also Dumberry and Rivoldini, 2015).

Downward heat transport from the outer liquid core into the thermally stratified inner core can also occur when energy generated by the dynamo process is dissipated ohmically in the inner core (Lister, 2003), but also this mechanism is thought to be inefficient (Labrosse, 2015).

The power that is available for sustaining a core dynamo originates from thermal and compositional buoyancy that drive convection in the core. Equations for estimating the available power for dynamo action from the power generated by buoyancy forces have been developed by assuming an adiabatic reference state and well-mixed light elements in the liquid core (Lister and Buffett, 1995; Lister, 2003; Gubbins et al., 2004; Labrosse, 2015). In some studies, however, these methods are applied for estimating the available power for dynamo action even though regions of the core are thermally stratified and an adiabatic reference state for the core is not always appropriate for all of the scenarios studied (Williams et al., 2007; Nimmo, 2007; Davies, 2015).

In this study, we develop a parameterised thermal evolution model for Mercury's mantle and core in which the mantle can transition smoothly from a convective state to a conductive state and we assess the influence of this transition on dynamo action in the core. We show that the use of an adiabatic temperature profile in thermally stratified regions can lead to an underestimation of the power available to drive the dynamo. We demonstrate that this can be avoided by implementing conductive heat transport in thermally stratified regions of the core irrespective of the mixing of light elements throughout the liquid core by fingering convection. Finally, we provide a set of thermal evolution scenarios to assess implications of Mercury's present-day magnetic field for the structure and composition of Mercury's core, the evolution and present-day dynamics of the mantle, and the temperature profile and thermal history of the planet.

2. Thermal evolution modelling

2.1. Methods

We separate the planet between a core and mantle, comprising distinct spherically symmetric layers in either conductive or convective state. We do not consider material exchange between mantle and core, nor do we consider long-term planetary contraction because its influence on the generation of heat and magnetic field is small (Lapwood, 1952; Gubbins et al., 2003). For these reasons, we assume that the planet's radius (R_p) and the core radius (R_c) are constant. Because the temperature profile and heat fluxes vary over time, the boundaries between conductive and convective layers in the mantle and core are also time dependent. Below, we develop a numerical scheme for the planet's thermal evolution, which additionally solves the rate of variation of these boundaries using energy balance principles.

We assume that Mercury's mantle is initially undergoing stagnant-lid convection (Breuer, 2011) and consists of a conductive lithosphere (volume V_{lm}) atop a convective mantle (volume V_{cm}) (Fig. 1). We write the temperature profile $T(t,r)$ in the mantle as:

$$T(t,r)=\begin{cases} T_{lm}(t,r), & \text{for } R_l(t)\le r\le R_p \\ T_{cm}(t,r), & \text{for } R_c\le r\le R_l(t) \end{cases} \tag{1}$$

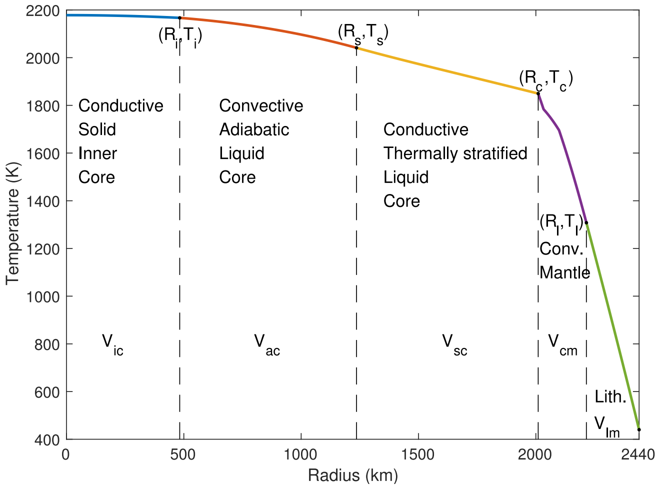

Fig. 1. The modelled temperature profile consisting of the conductive solid inner core (V_{ic}), adiabatic liquid core (V_{ac}), thermally stratified conductive liquid core (V_{sc}), convective mantle ('Conv. Mantle', V_{cm}), and lithosphere ('Lith', V_{lm}). This specific temperature profile and interior structure of the planet is a snapshot at 2.5 billion years after the start of the evolution of the baseline scenario (scenario 1 of Table 2). At this point in time, V_{cm} is in transition between convective and conductive state, and thermal boundary layers are distinguishable by the steep segments of the temperature profile in the upper and lower part of V_{cm}.

where R_l is the time-dependent boundary between the lithosphere with temperature profile T_{lm} and the convective region of the mantle with temperature profile T_{cm}, t is time, and r is the radial coordinate.

We only study thermal evolution scenarios in which the core solidifies from the planet's center upward and thermal stratification initiates at the CMB. Correspondingly, we separate the core in a solid inner core (volume V_{ic}), a thermally convective (adiabatic) liquid core layer (volume V_{ac}) and an outermost thermally stratified (conductive) liquid core layer (volume V_{sc}) (Fig. 1). We write the temperature profile of the core as:

$$T(t,r)=\begin{cases} T_{sc}(t,r), & \text{for } R_s(t)\le r\le R_c \\ T_{ac}(t,r), & \text{for } R_i(t)\le r\le R_s(t) \\ T_{ic}(t,r), & \text{for } 0\le r\le R_i(t) \end{cases} \tag{2}$$

where R_s is the time-dependent radial coordinate of the boundary between V_{ac} and V_{sc}, R_i is the time-dependent radius of the inner core, and T_{sc}, T_{ac}, and T_{ic} are the temperature profiles in V_{sc}, V_{ac}, and V_{ic}. We define the thermal energy of a layer of volume V_x with $x\in\{ic,ac,sc,cm,lm\}$ by

$$\mathscr{E}_x(t)=\int_{V_x(t)}\rho\, c\, T_x(t)\,\mathrm{d}V, \tag{3}$$

where ρ is the density and c is the specific heat capacity at constant composition and pressure. For the sake of simplicity, we assume that ρ and c are constant in the core ($\rho=\rho_c$ and $c=c_c$) and mantle ($\rho=\rho_m$ and $c=c_m$).

We now consider how thermal energies of the different subvolumes of Mercury change with time. For a volume that moves with the flow and always contains the same mass-elements (a so-called material volume V_M), we have the classical equation of conservation of energy, which we here express as

$$\frac{d\mathscr{E}(t)}{\mathrm{d}t}=-\int_{S_M(t)}(\vec{q}\cdot\vec{n})\mathrm{d}S+\int_{V_M(t)}\omega\,\mathrm{d}V, \tag{4}$$

where $\vec{q}$ is the heat flux vector, $\vec{n}$ is the outward pointing unit normal vector, ω is the total energy production in volume V_M per unit of time and volume, and S_M is the surface of V_M. Energy production in the mantle and in the core are specified in Section 2.2 and Section 2.3, respectively. Since the boundaries R_i, R_s, and R_l are time-dependent, we do not have a closed system and consider energy conservation over an arbitrary volume. For such a control volume V_C the Reynolds transport theorem states that

$$\frac{\mathrm{d}}{\mathrm{d}t}\int_{V_C(t)}\rho\, c\, T\,\mathrm{d}V=\int_{V_C(t)}\frac{\partial(\rho\, c\, T)}{\partial t}\,\mathrm{d}V+\int_{S_C(t)}\rho\, c\, T\left(\vec{v}_C\cdot\vec{n}\right)\mathrm{d}S, \tag{5}$$

where $\vec{v}_C$ is the velocity of the volume. For a material volume, Reynolds transport theorem gives

$$\frac{\mathrm{d}}{\mathrm{d}t}\int_{V_M(t)}\rho\, c\, T\,\mathrm{d}V=\int_{V_M(t)}\frac{\partial(\rho\, c\, T)}{\partial t}\,\mathrm{d}V+\int_{S_M(t)}\rho\, c\, T(\vec{v}\cdot\vec{n})\mathrm{d}S, \tag{6}$$

with $\vec{v}$ the flow velocity. By considering a time when $V_C(t)=V_M(t)$, we have by Eq. (4)

$$\begin{aligned}\frac{\mathrm{d}}{\mathrm{d}t}\int_{V_C(t)}\rho\, c\, T\,\mathrm{d}V=&-\int_{S_C(t)}(\vec{q}\cdot\vec{n})\mathrm{d}S+\int_{S_C(t)}\rho\, c\, T\left(\left(\vec{v}_C-\vec{v}\right)\cdot\vec{n}\right)\mathrm{d}S\\ &+\int_{V_C(t)}\omega\,\mathrm{d}V.\end{aligned} \tag{7}$$

At the long timescales of planetary evolution, we can set $\vec{v}=0$.

The derivatives of $\mathscr{E}_{lm}$ and $\mathscr{E}_{cm}$ with respect to time are now obtained from Eq. (7) and using that R_l is the only time-variable boundary of the considered volumes in the mantle:

$$\frac{\mathrm{d}\mathscr{E}_{lm}(t)}{\mathrm{d}t} = 4\pi\left(q_l R_l^2 - q_p R_p^2\right) + Q_{lm}(t) - \frac{\mathrm{d}R_l(t)}{\mathrm{d}t} 4\pi R_l^2 \rho_m c_m T_l(t), \tag{8}$$

and

$$\frac{\mathrm{d}\mathscr{E}_{cm}(t)}{\mathrm{d}t} = 4\pi\left(q_c R_c^2 - q_l R_l^2\right) + Q_{cm}(t) + \frac{\mathrm{d}R_l(t)}{\mathrm{d}t} 4\pi R_l^2 \rho_m c_m T_l(t), \tag{9}$$

where Q_{lm} and Q_{cm} are internal heat sources defined as the volume integrals of ω over V_{lm} and V_{cm}, q_c, q_l, and q_p are heat fluxes at R_c, R_l, and R_p in radial direction, and T_l is the temperature at R_l. To integrate Eqs. (8) and (9) with respect to time ($t \rightarrow t + \mathrm{d}t$), we need to determine $\mathrm{d}R_l/\mathrm{d}t$ (or equivalently $R_l(t + \mathrm{d}t)$). To do so, we parameterise $T_{lm}(t + \mathrm{d}t, r)$ and $T_{cm}(t + \mathrm{d}t, r)$ as functions of free parameters $R_l(t + \mathrm{d}t)$ and $T_l(t + \mathrm{d}t)$, as we describe in Section 2.2. With this parameterisation, we obtain values for $\mathscr{E}_{lm}(t + \mathrm{d}t)$ and $\mathscr{E}_{cm}(t + \mathrm{d}t)$ using Eq. (3). By equating those to the values for $\mathscr{E}_{lm}(t + \mathrm{d}t)$ and $\mathscr{E}_{cm}(t + \mathrm{d}t)$ obtained from Eqs. (8) and (9), we solve for the free parameters $R_l(t + \mathrm{d}t)$ and $T_l(t + \mathrm{d}t)$. The so-obtained temperature profiles $T_{lm}(t + \mathrm{d}t, r)$ and $T_{cm}(t + \mathrm{d}t, r)$ are strictly consistent with the energy balance by construction. As boundary conditions for the temperature profile of the mantle, we use a fixed surface temperature ($T(R_p, t) = T_p$), assume continuity of temperature and heat flux at R_l, and use the CMB temperature ($T(R_c) = T_c$) which is obtained from the thermal state of the core. The parameterisation of the temperature profile, heat transport, and heat production in the mantle are described in Section 2.2.

For the evolution of the core with moving boundaries R_i and R_s, we proceed as for the mantle and obtain

$$\frac{\mathrm{d}\mathscr{E}_{ic}(t)}{\mathrm{d}t} = -4\pi q_i R_i^2 + Q_{ic}(t) + \frac{\mathrm{d}R_i(t)}{\mathrm{d}t} 4\pi R_i^2 \rho_c c_c T_i(t), \tag{10}$$

$$\begin{aligned}\frac{\mathrm{d}\mathscr{E}_{ac}(t)}{\mathrm{d}t} = {} & 4\pi\left(q_i R_i^2 - q_s R_s^2\right) + Q_{ac}(t) + \frac{\mathrm{d}R_s(t)}{\mathrm{d}t} 4\pi R_s^2 \rho_c c_c T_s(t) \\ & - \frac{\mathrm{d}R_i(t)}{\mathrm{d}t} 4\pi R_i^2 \rho_c c_c T_i(t),\end{aligned} \tag{11}$$

and

$$\frac{\mathrm{d}\mathscr{E}_{sc}(t)}{\mathrm{d}t} = 4\pi\left(q_s R_s^2 - q_c R_c^2\right) + Q_{sc}(t) - \frac{\mathrm{d}R_s(t)}{\mathrm{d}t} 4\pi R_s^2 \rho_c c_c T_s(t), \tag{12}$$

where q_i and q_s are the heat fluxes at R_i and R_s, Q_{ic}, Q_{ac} and Q_{sc} are the internal heat sources in V_{ic}, V_{ac}, and V_{sc}, and T_i and T_s are the temperatures at R_i and R_s, respectively. To determine $R_i(t + \mathrm{d}t)$ and $R_s(t + \mathrm{d}t)$, we parameterise the temperature profiles T_{ic}, T_{ac}, and T_{sc} at $t = t + \mathrm{d}t$ as a function of four unknowns $R_i(t + \mathrm{d}t)$, $R_s(t + \mathrm{d}t)$, $T_i(t + \mathrm{d}t)$, and $T_s(t + \mathrm{d}t)$, as we describe in Section 2.3. We then solve for the four unknowns by equating values for $\mathscr{E}_{ic}(t + \mathrm{d}t)$, $\mathscr{E}_{ac}(t + \mathrm{d}t)$, and $\mathscr{E}_{sc}(t + \mathrm{d}t)$ obtained by Eqs. (10–12) to those obtained by Eq. (3) and use as a fourth equation that T_i equals a prescribed core liquidus profile T_{lc}:

$$T_{lc}(R_i(t + \mathrm{d}t)) = T_i(t + \mathrm{d}t). \tag{13}$$

As boundary conditions for T_{ic}, T_{ac}, and T_{sc} we use the heat flux q_c at R_c that is set by the mantle, the absence of heat flux at the planet's center, continuity of temperature and of heat flux at R_s, and continuity of temperature at R_i. The parameterisation of the temperature profile, heat transport and heat production in the core are described in Section 2.3.

2.2. *Temperature profile and heat sources in Mercury's mantle*

In this section, we describe the parameterisation of T_{cm}, T_{lm}, heat transport, and heat sources in the mantle. For clarity, we omit the time dependence of variables in the equations that follow, which hold for variables at the same t, and list all constants in Tables 1 and 2.

Table 1

Parameters used for thermal evolution scenarios. Parameter values subscripted by $_a$ are not used in Fig. 2, in which the CMB temperature evolves by Eq. (70) instead of by the core model of Section 2.3. The parameters subscripted by $_a$ are used in thermal evolution scenarios presented in Section 4. The solidus of the mantle by Namur et al. (2016b) is $T_{sol}(P) = 1421\mathrm{K} + 177\frac{\mathrm{K}}{\mathrm{GPa}}P - 12.2\frac{\mathrm{K}}{\mathrm{GPa}^2}P^2$.

Parameter	Symbol	Unit	value
Planet radius	R_p	km	2440
Surface temperature	T_p	K	440
Mantle density	ρ_m	$\mathrm{kg \cdot m^{-3}}$	3500, 3120_a
Mantle heat capacity	c_m	$\mathrm{J \cdot kg^{-1} \cdot K^{-1}}$	1142
Mantle thermal conductivity	k_m	$\mathrm{W \cdot m^{-1} \cdot K^{-1}}$	4
Mantle thermal expansivity	α_m	$\mathrm{K^{-1}}$	$2.5 \cdot 10^{-5}$
Mantle's gravity	g_m	$\mathrm{m \cdot s^{-2}}$	3.7
Activation energy	A	$\mathrm{J \cdot mol^{-1}}$	$3 \cdot 10^{5}$
Reference viscosity	η_{ref}	Pa·s	10^{21}
Reference Temperature	T_{ref}	K	1600
Present-day ^{40}K in mantle	$X_{^{40}\mathrm{K}}$	ppm	400
Present-day ^{232}Th in mantle	$X_{^{232}\mathrm{Th}}$	ppb	50
Present-day ^{235}U in mantle	$X_{^{235}\mathrm{U}}$	ppb	0.2016
Present-day ^{238}U in mantle	$X_{^{238}\mathrm{U}}$	ppb	27.7984
Average lifetime of ^{40}K	$\tau_{^{40}\mathrm{K}}$	Gyr	1.8
Average lifetime of ^{232}Th	$\tau_{^{232}\mathrm{Th}}$	Gyr	20.2
Average lifetime of ^{235}U	$\tau_{^{235}\mathrm{U}}$	Gyr	1.02
Average lifetime of ^{238}U	$\tau_{^{238}\mathrm{U}}$	Gyr	6.45
Heating coefficient of ^{40}K	$I_{^{40}\mathrm{K}}$	$\mathrm{W \cdot kg^{-1}}$	$3.247 \cdot 10^{-9}$
Heating coefficient of ^{232}Th	$I_{^{232}\mathrm{Th}}$	$\mathrm{W \cdot kg^{-1}}$	$28.998 \cdot 10^{-6}$
Heating coefficient of ^{235}U	$I_{^{235}\mathrm{U}}$	$\mathrm{W \cdot kg^{-1}}$	$576.5 \cdot 10^{-6}$
Heating coefficient of ^{238}U	$I_{^{238}\mathrm{U}}$	$\mathrm{W \cdot kg^{-1}}$	$90.79 \cdot 10^{-6}$
Initial mantle temperature	$T_m(t = 0)$	K	1750
Initial lithosphere radius	$R_l(t = 0)$	km	2400, 2360_a
Scaling parameter	β_b	–	$\frac{1}{3}$
Scaling parameter	β_u	–	2.1
Scaling parameter	x_1	–	0.53
Scaling parameter	x_2	–	2
Critical Rayleigh number	Ra_{crit}	–	450
Scaling parameter	a_{rh}	–	5.1
Core thermal conductivity	k_c	$\mathrm{W \cdot m^{-1} \cdot K^{-1}}$	45_a
Core latent heat	L	$\mathrm{kJ \cdot kg^{-1}}$	300_a
Present-day ^{40}K in core	$X_{^{40}\mathrm{K,c}}$	ppm	8_a
Adiabatic parameter	τ_2	$\mathrm{K \cdot m^{-2}}$	$-2.8 \cdot 10^{-14}_a$
Adiabatic parameter	τ_3	$\mathrm{K \cdot m^{-3}}$	$-1.2 \cdot 10^{-20}_a$
Initial CMB temperature	$T_c(t = 0)$	K	2000, 2100_a
Core radius	R_c	km	2010
Core density	ρ_c	$\mathrm{kg \cdot m^{-3}}$	7200
Core heat capacity	c_c	$\mathrm{J \cdot kg^{-1} \cdot K^{-1}}$	840
Compositional expansion coefficient	β_X	–	0.9_a
Compositional fractionation coefficient	D_l^s	–	0.9_a
Liquidus parameter	$T_{cl,1}$	K	1991_a
Liquidus parameter	$P_{cl,1}$	GPa	5.2_a
Liquidus parameter	$P_{cl,2}$	GPa	21.5_a

Mantle convection simulations, experiments, and theory show that the temperature profile T_{cm} is steep in thermal boundary layers at the top and bottom of the convective volume and shallow in the vigorously convective region between the thermal boundary layers (e.g. Grasset and Parmentier, 1998; Davaille and Jaupart, 1993; Schubert et al., 2001). Due to the cooling of the mantle, the increase of the temperature-dependent viscosity, and the decrease of the temperature differences across the mantle, convection weakens, thermal boundary layers grow, and the mantle's temperature profile gradually converges to a conductive profile (Thiriet et al., 2019). To model the transition from convective to a conductive state in V_{cm}, we model T_{cm} as a superposition of a convective and conductive temperature profile

$$T_{cm}(r) = \lambda T_{cm,\mathrm{conv}}(r) + (1 - \lambda) T_{cm,\mathrm{cond}}(r), \tag{14}$$

where the parameter $\lambda = 1$ when thermal boundary layers are thin, λ decreases from 1 to 0 as thermal boundary layers become large, and $\lambda = 0$ when all heat transport through the mantle occurs by conduction. The heat fluxes at R_l and R_c are computed as $q_{l/c} = -k_m \nabla T_{cm}(R_{l/c})$, with k_m the thermal conductivity of the mantle. It follows that $q_{l/c} = \lambda q_{l/c,\mathrm{conv}} + (1 - \lambda) q_{l/c,\mathrm{cond}}$ with $q_{l/c,\mathrm{conv/cond}} = -k_m \nabla T_{cm,\mathrm{cond/conv}}(R_{l/c})$. We see that

Table 2

Characteristics of thermal evolution scenarios using parameters and initial conditions of Table 1. The first 5 rows denote initial conditions and parameter values of the thermal evolution scenarios. Time at which core solidification begins is denoted by $t_{R_i>0}$. Time at which the thermal boundary layers in the mantle touch (when $\lambda = 0$) is denoted by $t_{\lambda=0}$. Time at which the modelled transition from mantle's convective state to conductive state initiates (when $\lambda < 1$) is denoted by $t_{\lambda<1}$. Time at which the partial melt zone in the mantle closes is denoted by $t(T < T_{sol})$ and time at which the mantle is everywhere cooler than $T_{sol} + 75\text{K}$ is denoted by $t(T < T_{sol} + 75\text{K})$. Other rows gives variable values at present. Q_i is the total conductive heat loss from the inner core. Heat release by radiogenic decay and secular cooling in the liquid core are denoted by Q_H and Q_S. Definitions of entropy production E_L, E_i, $E_{G,ac}$, $E_{G,sc}$, E_H and E_S, and of the conductive entropy sink E_k, are given in Appendix D (note that E_H is given in units of kW/K). E_{ac} and E_{sc} respectively denote entropy production in V_{ac} and V_{sc} that is available for dissipation.

Variable	Scenario 1	Scenario 2	Scenario 3	Scenario 4	Scenario 5	Scenario 6	Scenario 7
X_c(wt%)	9	3.6	10	9	9	6	6
$\frac{dT_{cl}}{dX}$ (K/wt%)	50	150	50	50	50	50	50
D_l^s	0.9	0.9	0.5	0.9	0.9	0.9	0.9
η_0 (Pa·s)	10^{21}	10^{21}	10^{21}	10^{20}	10^{22}	10^{20}	10^{22}
γ_{rad}	0.2	0.2	0.2	2.0	0.4	2.0	1
$t_{R_i>0}$ (Gyr)	2.2	2.9	2.6	2.8	3.0	1.6	1.8
$t_{\lambda=0}$ (Gyr)	3.7	3.6	3.6	–	2.9	–	–
$t_{\lambda<1}$ (Gyr)	1.6	1.6	1.6	–	0	–	1.8
$t(T < T_{sol})$ (Gyr)	1.2	1.2	1.2	3.5	2.3	3.8	3.3
$t(T < T_{sol} + 75\text{K}$ (Gyr)	0.8	0.8	0.8	3.0	1.0	3.1	2.3
$T_c(t = 4.5Gyr)$ (K)	1727	1690	1703	1771	1786	1812	1923
$T_{center}(t = 4.5Gyr)$ (K)	2048	2019	2031	2099	2126	2141	2224
$T_s(t = 4.5Gyr)$ (K)	1871	1846	1868	1930	1957	1945	2102
$T_i(t = 4.5Gyr)$ (K)	1968	1973	1981	2046	2087	2013	2173
$R_i(t = 4.5Gyr)$ (km)	1254	981	998	1039	896	1491	1117
$R_s(t = 4.5Gyr)$ (km)	1561	1480	1444	1467	1424	1661	1365
$q_c(t = 4.5Gyr)$ (mW/m^2)	12.9	12.2	12.4	11.7	12.3	15.4	11.2
$X_{oc}(t = 4.5Gyr)$(wt%)	9.25	3.64	10.67	9.13	9.08	6.32	6.11
Q_c (GW)	654	618	629	594	624	781	570
Q_L (GW)	339	286	212	290	271	415	259
Q_G (GW)	12.6	5.4	57	13	13	7.6	7.3
Q_i (GW)	112	51	56	62	39	217	64
Q_H (GW)	1.0	1.1	1.1	11	2.3	7.5	5.3
Q_S (GW)	189	273	302	218	299	134	235
E_L (MW/K)	9.0	10.0	6.5	8.6	8.6	7.1	4.0
$E_{G,ac}$ (MW/K)	3.8	1.8	17.3	3.8	4.0	1.9	1.3
$E_{G,sc}$ (MW/K)	3.1	1.2	14.0	3.1	3.0	2.1	2.3
E_i (MW/K)	3.0	1.8	1.7	1.8	1.2	3.7	1.0
E_H (kW/K)	3.8	6.2	4.8	47	11	17	7
E_S (MW/K)	0.7	1.2	1.2	0.8	0.9	0.3	0.2
E_k (MW/K)	9.8	8.6	7.2	7.8	7.0	9.8	4.0
E_Φ (MW/K)	9.6	7.6	33.8	10.3	10.8	5.4	4.8
E_T (MW/K)	2.9	4.6	2.6	3.4	3.8	1.4	1.2
E_X (MW/K)	6.7	3.0	31.3	6.9	7.0	4.0	3.6
E_{ac} (MW/K)	6.6	6.4	19.9	7.2	7.8	3.3	2.5
E_{sc} (MW/K)	3.1	1.2	14.0	3.1	3.0	2.1	2.3

the modelled transport of heat through the mantle varies from the convective flux $q_{l/c} = q_{l/c,\text{conv}}$ to the conductive flux $q_{l/c} = q_{l/c,\text{cond}}$ as λ runs from 1 to 0. We first parameterise $T_{cm,\text{conv}}$ and $T_{cm,\text{cond}}$ and afterwards describe how we vary λ with time.

We parameterise $T_{cm,\text{conv}}$ as done by Thiriet et al. (2019).

$$T_{cm,\text{conv}}(r) = \begin{cases} T_c + \dfrac{T_m - T_c}{\delta_b}(r - R_c), & \text{for } R_c \le r \le R_b \\ T_m, & \text{for } R_b \le r \le R_u \\ T_m + \dfrac{T_l - T_m}{\delta_u}(r - R_u), & \text{for } R_u \le r \le R_l \end{cases}, \tag{15}$$

where δ_b and δ_u are the thicknesses of thermal boundary layers at the bottom and at the top in V_{cm}, $R_b = R_c + \delta_b$, and $R_u = R_l - \delta_u$. Expressions for $q_{c,\text{conv}}$ and $q_{l,\text{conv}}$ as well as for the thermal energy associated to these temperature profiles are given in Appendix A.

The upper thermal boundary layer is much thicker than the lower thermal boundary layer as a result of its lower temperature and higher viscosity (Thiriet et al., 2019). For this reason, and because the heat fluxes through the thermal boundary layers are related to the thermal gradients in these boundary layers, the parameterisation of the thickness of and the temperature difference across the upper thermal boundary layer largely determines the efficiency of heat transport through V_{cm}. We parameterise the thermal boundary layers as is done in Thiriet et al. (2019), see Appendix A. In this model, δ_u depends on a parameter β^u by

$$\delta_u = (R_l - R_c)\left(\frac{Ra_{crit}}{Ra_u}\right)^{\beta^u}, \tag{16}$$

where Ra_{crit} (described by Eq. (A.6)) and Ra_u (described by Eq. (A.3)) are the critical Rayleigh number and a Rayleigh number for the upper thermal boundary layer. The temperature difference across the upper thermal boundary layer depends on a parameter a_{rh} (Thiriet et al., 2019) by

$$T_m - T_l = \frac{a_{rh}\mathcal{R}T_m^2}{A}, \tag{17}$$

where $\mathcal{R}$ is the ideal gas constant and A is an activation constant. Thiriet et al. (2019) found that they could reproduce the thermal evolution of numerical mantle convection simulations with their parameterised thermal evolution model by setting $\beta^u = 0.335$ and $a_{rh} = 2.54$. Our thermal evolution model is different from that of Thiriet et al. (2019). For example, we determine the time-variation of R_l by enforcing a strict energy balance of V_{lm} and V_{cm} and integrate the corresponding temperature profiles of these volumes for this purpose, as is described in Section 2.1. Furthermore, in the lithosphere we adopt an analytical solution of the conduction equation which is described below. If we use identical values for β^u and a_{rh} as Thiriet et al. (2019) in our thermal evolution model with also identical values for other model parameters, we obtain a lower q_c and faster cooling rate of the mantle as compared that obtained by the parameterised thermal evolution model of Thiriet et al. (2019) (Fig. 2). We have therefore estimated the values of β^u and a_{rh} for which our model best reproduces a mantle convection simulation. We have employed the Gaia mantle convection code in spherical annulus geometry setup (Hüttig et al., 2013; Fleuri et al., 2024) to simulate a thermal evolution scenario using planetary and material parameters identical to those used in Thiriet et al. (2019). The thermal evolution of average mantle temperature and CMB and surface heat flow (q_c and q_p) obtained by Gaia can be best reproduced with our model using parameter values $\beta^u = 0.21$ and $a_{rh} = 5.1$ (Fig. 2 and B.9, see Appendix B for details). Reasons for obtaining different best-fit values for β^u and a_{rh} as compared to Thiriet et al. (2019) are partly related to differences between the parameterised thermal evolution models and partly related to adopting spherical annulus geometry for our 2D mantle simulation whereas 3D spherical geometry has been used by Thiriet et al. (2019). Setting $\beta^u = 0.25$ and $a_{rh} = 4.0$ with our thermal evolution model yields a best-fit to the 3D simulation of Thiriet et al. (2019). In this study, we set $\beta^u = 0.21$ and $a_{rh} = 5.1$. The evolution of the temperature profile of the mantle obtained by our Gaia mantle convection simulation and our parameterised thermal evolution model are compared in Fig. B.9.

We parameterise $T_{cm,cond}$ by the steady-flux solution of the conduction equation for a spherical shell, in terms of three parameters (Lister and Buffett, 1998; Knibbe and van Westrenen, 2018):

$$T_{cm,\text{cond}}(r) = -\frac{S_{cm}}{6k_m}r^2 + \frac{A_{cm}}{r} + B_{cm}, \tag{18}$$

where S_{cm} is the volume-averaged secular cooling of V_{cm}. This steady-flux solution is valid if heat fluxes at the boundaries of V_{cm} are constant over time and, consequently, the cooling rate is uniform and S_{cm} is independent of radius. Knibbe and Van Hoolst (2021) showed that using this temperature profile for a conductive spherical shell in which the heat fluxes slowly evolve over time, and correspondingly the radial variation of secular cooling is small, leads to insignificant errors in the obtained thermal evolution compared to the solution of the unsteady conduction problem. Because heat fluxes slowly evolve over time, parameters S_{cm}, A_{cm}, and B_{cm} are time dependent. Their values are determined using the temperature boundary conditions T_l and T_c and by relating this temperature profile to the estimate for $\mathscr{E}_{cm}$ which is obtained by using Eq. (3) on $T_{cm,\text{conv}}$. Expressions for S_{cm}, A_{cm}, and B_{cm} and for heat fluxes $q_{c,\text{cond}}$ and $q_{l,\text{cond}}$ are given in Appendix A.

Because the transition in the mantle from convective to conductive state proceeds gradually over time (Guerrero et al., 2021), we aim for a smooth temporal variation of λ. Various time-dependent parameterisations for λ can describe the transition from convective to conductive state of the mantle. By trial and error we found that we can reproduce the evolution of the average mantle temperature and the heat fluxes q_c and q_p obtained by Gaia by describing λ by

$$\lambda = \begin{cases} 1, & \text{for } x_1(R_l - R_c) \le R_u - R_b \\ \frac{1}{2} + \frac{1}{2}cos\left(\pi\left[1 - \left(\frac{R_u - R_b}{x_1(R_l - R_c)}\right)^{x_2}\right]\right), & \text{for } 0 \le R_u - R_b \le x_1(R_l - R_c) \\ 0, & \text{for } R_u - R_b \le 0 \end{cases} \tag{19}$$

Parameter x_1 determines the value of $(R_u - R_b)/(R_l - R_c)$ at the moment in time when λ transitions from 1 to a value below 1. From then on, the mantle begins its transition to a conductive state and the temperature profile in the convective region of the mantle (T_{cm}) is given by a combination of the piecewise linear temperature profile $T_{cm,\text{conv}}$ and the conductive temperature profile $T_{cm,\text{cond}}$ (see Eq. (14)). Parameter x_1, thus, determines when the mantle begins its transition to a conductive state based on the relative thickness of the two thermal boundary layers combined. A small value of x_1 of 0.2, for example, leads to a late beginning of the transition to a conductive state in which the parameterised evolution diverges from the evolution obtained by Gaia from

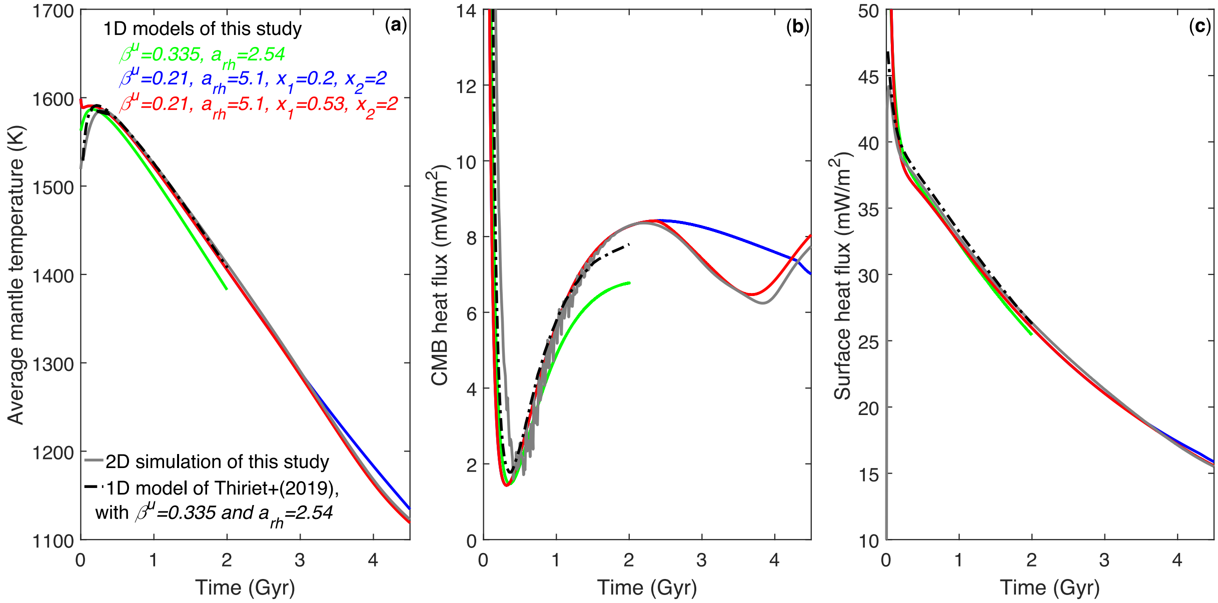

Fig. 2. Average mantle temperature (a), CMB heat flux (q_c) (b), and surface heat flux (q_p) (c). 2D thermal convection simulation (solid black), parameterised evolution models in green, blue and red. In blue and red scenarios, parameter values $\beta^u = 0.21$, $a_{rh} = 5.1$ and $x_2 = 2$ are adopted. In the blue scenario, parameter x_1 is set at 0.2, such that the transition in the mantle initiates when thermal boundary layers make up 80% of the convective region of the mantle, which occurs at about 4.2 Gyr. Parameter x_1 is set at 0.53 in the red scenario such that the transition from convective to conductive heat transfer of the mantle initiates when thermal boundary layers consume almost half of the convective region of the mantle, which occurs at about 2.3 Gyr. $\beta^u = 0.335$ and $a_{rh} = 2.54$ from Thiriet et al. (2019) are adopted in the thermal evolution model plotted in green. This thermal evolution scenario is shown to compare our thermal evolution model to that of Thiriet et al. (2019) which runs for 2 Gyr using identical parameter values (data taken from Fig. S5 of their supplementary information) (dashed-dotted black line). For this reason, also the green thermal evolution scenario is stopped at 2 Gyr. (For interpretation of the references to colour in this figure legend, the reader is referred to the web version of this article.)

about 2.3 Gyr onwards (Fig. 2). We set x_1 to 0.53, which is the value of $(R_u - R_b)/(R_l - R_c)$ of the thermal evolution scenario at about 2.3 Gyr. Parameter x_2 controls how rapidly the transition from convective to conductive state proceeds. For $x_2 > 1$, the transition to a conductive state proceeds rapidly after the temperature profile begins to deviate from parameterised convection. For $x_2 < 1$, the transition is more slowly and continues until the boundary layers cover a large portion of V_{cm}. The 2D mantle convection simulation by Gaia is reproduced accurately by our parameterised thermal evolution model with $x_1 = 0.53$ and $x_2 = 2$ (Figs. 2 and B.9).

The steady flux solution for conduction of a spherical shell (Eq. 18) can also be used for the temperature profile T_{lm}. However, because the surface temperature T_p is assumed constant and temperature at depth varies over time, the cooling rate must vary with depth in V_{lm}. We therefore use two constraints on S_{lm}, which denotes the secular cooling in the lithosphere, to improve the parameterisation of T_{lm} (Eq. 18). First, the integral of S_{lm} over V_{lm} must be consistent with the lithosphere's energy balance, and second S_{lm} must be equal to the local internal heat production at T_p since T_p is constant over time. We adopt a simple linear radial variation of S_{lm} with depth

$$S_{lm}(r) = \rho_m H_m + s_{lm}(R_p - r), \tag{20}$$

where H_m is the radiogenic energy production per unit of mass in the mantle, which we assume to be volumetrically uniform. For such a radial profile of S_{lm}, the temperature profile T_{lm} becomes

$$T_{lm}(r) = \frac{\rho_m H_m + s_{lm}(R_p - r)}{6k_m} r^2 + \frac{A_{lm}}{r} + B_{lm}. \tag{21}$$

Variables s_{lm}, A_{lm} and B_{lm} are solved using boundary conditions $T_{lm}(R_p) = T_p$, $T_{lm}(R_l) = T_l$, and the heat flux continuity boundary condition $-k_m \nabla T_{lm}(R_l) = q_l$. Expressions for these variables, for the thermal energy associated to this temperature profile, and for q_p are listed in Appendix A.

We have tested the effect of adopting a uniform S_{lm} for the steady-flux approximation of the conductive temperature profile (Eq. 18) instead of varying S_{lm} with depth as in Eq. (21) and found that the thermal evolution is insensitive to this choice (see Fig. A.7 in Appendix B). We adopt the linear variation with depth of S_{lm} as described above for consistency with the assumed fixed surface temperature of the planet.

We account for heat production in the mantle per unit mass H_m by radioactive decay of isotopes ^{232}Th, ^{40}K, ^{235}U and ^{238}U. We model radiogenic isotopes to be uniformly distributed across the mantle and discuss their abundances in Section 3. Expressions for H_m and for Q_{cm} and Q_{lm} are given in Appendix A.

2.3. Thermal structure and heat sources in Mercury's core

In Section 2.3.1, we parameterise temperature profiles T_{ic}, T_{ac}, and T_{sc} and define the heat fluxes q_i and q_s between the corresponding layers of the core. In Section 2.3.2, we describe the compositional profile of the core and the associated flux of light elements through the core. Heat sources and sinks in the core are described in Section 2.3.3 and a formulation for the entropy production that is available for ohmic dissipation is given in Section 2.3.4.

2.3.1. The temperature profile of the core

We assume that heat is transported by conduction in V_{ic} and V_{sc} because the heat flux is subadiabatic in these regions and we describe T_{ic} and T_{sc} by a steady-flux conductive temperature profile similar to Eq. (18). The expressions for the coefficients of these temperature profiles, the thermal energy associated to these profiles, and the fluxes $q_{i/s} = -k_c \nabla T(R_{i/s})$, with k_c the thermal conductivity of the core which we assume constant, are listed in Appendix C.

We describe T_{ac} by an adiabat. The adiabatic gradient is

$$\frac{\mathrm{d}T_{ad}(r)}{\mathrm{d}r} = -\frac{\alpha_c(r) g(r)}{c_c} T_{ac}(r), \tag{22}$$

where α_c is the thermal expansion and

$$g(r) = \frac{4\pi}{3} G \rho_c r \tag{23}$$

is the local gravity. Thermal expansion is a radially dependent variable that decreases with increase of pressure by a factor of about 2 in Mercury's core (Fig. C.10).

We parameterise the adiabat by

$$T_{ac}(r) = T_0 \left(1 + \sum_{j=1}^{n} \tau_j r^j \right), \tag{24}$$

where T_0 is the time-dependent reference temperature at the planet's center and τ_j with $j = 1, \ldots, n$ describe the radial variation of the adiabat. The coefficients τ_j for $j > 1$ are constants since ρ_c, c_c and α_c are time independent, and can be determined from the identity of the right-hand side of Eqs. (22) and (24). Because $g(0) = 0$, we have $\mathrm{d}T_{ad}(r)/\mathrm{d}r = 0$ at the planet's center. To meet this property of the adiabat expressed by Eq. (24), we require that $\mathrm{d}T_{ac}(r = 0)/\mathrm{d}r = \tau_1 T_0 = 0$, which implies that $\tau_1 = 0$. In this study, we set $n = 3$ and determine τ_2 and τ_3 in Section 3.2 by fitting Eq. (24) to a reference adiabat for Mercury's core based on assumed values for $\alpha_c(r)$, c_c and ρ_c.

Following Knibbe and van Westrenen (2018), we introduce $\epsilon(r)$ as the ratio of the volume-averaged adiabatic temperature profile in a sphere of radius r normalised by the temperature at the sphere's surface

$$\epsilon(r) = \frac{1 + \sum_{j=2}^{n} \frac{3}{3+j} \tau_j r^j}{1 + \sum_{j=2}^{n} \tau_j r^j}, \tag{25}$$

which is constant in time. The thermal energy of V_{ac} is then conveniently given by

$$\mathscr{E}_{ac} = \frac{4\pi}{3} R_s^3 \epsilon(R_s) \rho_c c_c T_s - \frac{4\pi}{3} R_i^3 \epsilon(R_i) \rho_c c_c T_i. \tag{26}$$

The thermal evolution scenarios of this study begin with a fully liquid superheated core and an adiabatic temperature profile. The heat flux is initially superadiabatic throughout the liquid core. During the early thermal evolution, both the temperature and heat flux in the core decrease with time. Thermal stratification in the liquid core initiates where the heat flux first drops below $-k_c \nabla T_{ac}$. In the scenarios of this study, this occurs at the CMB.

2.3.2. Radial profile and flux of light element

The rate of solidification of the core and the entropy production available for dynamo action depends on fractionation of light elements during inner core solidification and the subsequent mixing of these elements throughout the core. To account for the fractionation and transport of light elements in the core, we model the profile of light element weight fraction X as a function of radius as

$$X(r) = \begin{cases} X_{ic}(r), & \text{for } r \le R_i \\ X_{oc}, & \text{for } R_i \le r \le R_c \end{cases} \tag{27}$$

with X_{oc} the light element fraction in the liquid core and $X_{ic}(r)$ the profile of light element fraction in the solid inner core. Because we assume that light elements are well mixed throughout the liquid core, X_{oc} is independent of radius and written as

$$X_{oc} = \frac{M_{l,oc}}{M_{oc}}, \tag{28}$$

with M_{oc} the total mass of the liquid core and $M_{l,oc}$ the total mass of light elements in the liquid core. We assume that the inner core solidifies by a fractional crystallisation process. At R_i, we have

$$X_{ic}(R_i) = D_l^s X_{oc}, \tag{29}$$

with D_l^s the partitioning coefficient of the light element between solid and liquid metal. We obtain the expression for the mass flux of the light element q_X by equating the mass flux of light elements into a spherical layer that is bounded by above by R_c to the time variation of the mass of light elements in that layer

$$q_X(r)4\pi r^2 = \frac{\mathrm{d}X_{oc}}{\mathrm{d}t}\rho_c\frac{4\pi}{3}\left(R_c^3 - r^3\right). \tag{30}$$

Differentiating Eq. (28) with respect to time gives

$$\frac{\mathrm{d}X_{oc}}{\mathrm{d}t} = \frac{\mathrm{d}M_{l,oc}}{\mathrm{d}t}\frac{1}{M_{oc}} - \frac{\mathrm{d}M_{oc}}{\mathrm{d}t}\frac{M_{l,oc}}{M_{oc}^2}. \tag{31}$$

Because density is assumed constant, the time derivatives on the right-hand side can be written in terms of the growth rate of the inner core

$$\frac{\mathrm{d}M_{oc}}{\mathrm{d}t} = -\rho_c 4\pi R_i^2\frac{\mathrm{d}R_i}{\mathrm{d}t} \tag{32}$$

and

$$\frac{\mathrm{d}M_{l,oc}}{\mathrm{d}t} = -D_l^s X_{oc}\rho_c 4\pi R_i^2\frac{\mathrm{d}R_i}{\mathrm{d}t}. \tag{33}$$

The time-evolution of X_{oc} and q_X can be obtained by integrating Eq. (31) over time. This method is also valid if D_l^s varies during the evolution, for example as a function of composition, temperature or pressure. If D_l^s is constant over time, the integration can be done analytically and yields the Scheil-Gulliver equation (Scheil, 1942)

$$X_{oc} = \frac{M_l}{M_c}\left(\frac{M_{oc}}{M_c}\right)^{D_l^s - 1}, \tag{34}$$

with M_c the total mass of the core and M_l the mass of light elements in the core.

2.3.3. Energy sources in the core

For radiogenic production of heat in the core, we include only potassium as significant radioactive core constituent at ppm concentrations of 1/50th relative to the mantle, because other radiogenic elements are expected to be present in the core at even smaller amounts (Boujibar et al., 2019).

The production of latent heat by solidification of the inner core is given by

$$Q_L = L\rho_c 4\pi R_i^2\frac{\mathrm{d}R_i}{\mathrm{d}t}, \tag{35}$$

where L is the latent heat due to the phase change of solidification per unit of mass (Lister and Buffett, 1995).

On timescales of tens of million years to billion years relevant for the planet's long-term evolution, the rate of dissipative heat release Φ balances the rate of work done by buoyancy forces (Lister and Buffett, 1995; Labrosse, 2015)

$$\Phi = \int_{V_c}\phi\,\mathrm{d}V = \int_{V_c}\left(F_X + F_T\right)\mathrm{d}V. \tag{36}$$

Here, ϕ is the local production rate of heat by viscous and ohmic dissipation, $F_X = -q_X^*\beta_X\nabla\psi$ and $F_T = -q_T^*\cdot\nabla T/T$ are the rate of work done by compositional and thermal buoyancy forces, respectively, with q_X^* and q_T^* the convective fluxes of light elements and heat, the gravitational potential is denoted by ψ ($g = -\nabla\psi$), and β_X is the compositional expansion coefficient:

$$\beta_X = -\frac{1}{\rho_c}\frac{\partial\rho_c}{\partial X}\bigg|_{P,T}. \tag{37}$$

We see from the definition of F_T that the dissipation associated with work done by thermal buoyancy is the release of heat that initially belonged to the thermal energy of the core. This dissipation relates to transport of heat within V_{ac} and is implicitly accounted for by implementing an adiabatic temperature profile T_{ac}. By the definition of F_X we see that the rate of work done by compositional buoyancy equals the dissipation of energy that was initially stored in the gravitational potential. Therefore it contributes to the thermal energy of the core. The conversion of gravitational energy to heat is independent of whether the light elements are transported by diffusion or convection, but only the convective flux of light elements contributes to viscous and ohmic dissipation (Lister and Buffett, 1995). Here we assume that all transport of light elements occurs by convection because compositional diffusivity is small (Lister and Buffett, 1995; Nimmo, 2007), such that q_X^* can be approximated by q_X. We write the release of gravitational energy as heat in V_{ac} and in V_{sc} as

$$Q_{G,ac} = \int_{V_{ac}}\phi_X\,\mathrm{d}V \tag{38}$$

and

$$Q_{G,sc} = \int_{V_{sc}}\phi_X\,\mathrm{d}V, \tag{39}$$

with ϕ_X the local dissipative heat release of gravitational energy due to the redistribution of light elements. Because $Q_{G,ac}$ contributes to Q_{ac} and $Q_{G,sc}$ contributes to Q_{sc}, an assumption on how ϕ_X is distributed between V_{ac} and V_{sc} is needed to model the planet's thermal evolution. The distribution of ϕ_X is not known and must be studied by magnetohydrodynamical convection simulations (Lister and Buffett, 1995). Here, we assume that ϕ_X is locally equal to the work performed by compositional buoyancy

$$\phi_X(r) = F_X(r). \tag{40}$$

Q_{ic}, Q_{ac}, and Q_{sc} can now be written as the sum of the heat sources described above, and are listed in Appendix C. This completes the planet's thermal evolution model.

2.3.4. The entropy production available for dynamo action

The evolution of the magnetic field can be assessed by using Eq. (36), which yields the power that is available for viscous and ohmic dissipation. Because of the low viscosity of metallic liquid, the viscous dissipation in a planetary core is small and Φ is commonly only ascribed to ohmic dissipation. A necessary condition for sustaining a magnetic field is that $\Phi > 0$ (Gubbins et al., 2004).

We recall that the magnetic field of Mercury is likely generated in a convective layer deep below a stably stratified layer of the liquid core, and that large amount of light-element transport through double-diffusive convection in the thermally stratified layer can effect the magnetic field (Manglik et al., 2010; Takahashi et al., 2019). To relate thermal evolution scenarios to these aspects of the magnetic field, it is useful to separately assess ohmic dissipation in V_{ac} and in V_{sc} and separately determine the ohmic dissipation associated with F_X and F_T. This can be achieved by performing the integral of Eq. (36) over V_{ac} and V_{sc}, and by performing the integration of F_X and F_T separately in Eq. (36).

Often, the rate of entropy production that is available for ohmic dissipation E_Φ is reported in thermal evolution studies instead of the work done by buoyancy forces (Gubbins et al., 2004; Labrosse, 2015; Davies, 2015; Greenwood et al., 2021a). These studies do not explicitly express E_Φ in terms of F_X and F_T, but we show in Appendix D that

$$E_{\Phi} = \int_{V_c} \left(\frac{F_X}{T} + \frac{F_T}{T} \right) \mathrm{d}V. \tag{41}$$

Consequently, it is straightforward to define E_{ac} and E_{sc} as the entropy production available for dissipation in V_{ac} and V_{sc}, and to define E_X and E_T as the entropy production associated with F_X and F_T, respectively. Because we implemented a conductive temperature profile and the compositional profile in the inner core is stable, we have $F_X = F_T = 0$ in the inner core and $E_{ic} = 0$. Furthermore, $F_T = 0$ in V_{sc} because we implemented a conductive temperature profile in that region.

We now clarify the implications on the ohmic dissipation if an adiabatic temperature profile is assumed in a thermally stratified region of the core. Because F_T is given by

$$F_T = -q_T^{*} \cdot \frac{\nabla T}{T} = -(q_T - q_k) \cdot \frac{\nabla T}{T} \tag{42}$$

with q_T the local heat flux and q_k the local conductive heat flux, we locally have $q_k > q_T$ and $F_T < 0$ if an adiabat is implemented in a thermally stratified region. This negative work done by thermal buoyancy implies that a downward convective heat flux consumes entropy that would otherwise be available for ohmic dissipation. For this reason, if an adiabat is implemented in a thermally stratified region where a downward convective heat flux is not expected, Φ and E_{Φ} will be underestimated. For some thermal evolution scenarios, Φ and E_{Φ} may become negative, conflicting with the second law of thermodynamics. In Section 4.1 we will compare our thermal evolution model with a thermal evolution model in which an adiabat is adopted in the entire core to quantify the influence of this choice.

3. Parameter values for Mercury

In Section 3.1 and Section 3.2, we describe the parameter values that are used in the thermal evolution scenarios for the mantle and core. We will produce a 'baseline thermal evolution scenario' by the method described in the previous sections using model parameters listed in Table 1 and listed in Table 2 as scenario 1. This scenario is used to describe the general behaviour of Mercury's thermal evolution and to illustrate the influence of the transition from convective to conductive state of the mantle on the evolution of the entropy production available for the dynamo.

We will compare this baseline scenario to an 'adiabatic core model' in which the entire core is assumed to be adiabatic, as has long been common practice in thermal evolution studies of Mercury (Stevenson et al., 1983; Michel et al., 2013; Tosi et al., 2013a). Hence, in this adiabatic core model, T_{ac}, T_{sc}, and T_{ic} are all parameterised by Eq. (24). We additionally compare the baseline model to an 'adiabatic inner core model' in which T_{sc} is given by the conductive temperature profile as in the baseline model but in which both T_{ac} and T_{ic} are parameterised by Eq. (24), as done in Knibbe and van Westrenen (2018), Knibbe and Van Hoolst (2021), and Greenwood et al. (2021a). We perform these comparisons to test how sensitive modelling the thermal evolution of Mercury is to the various assumptions for the core's temperature profile that are adopted in literature.

Finally, we vary several model parameters of the core and mantle to investigate how they affect the thermal evolution of Mercury and its magnetic field generation.

3.1. Parameters of Mercury's mantle

We adopt most of the parameter values for Mercury's mantle used by Thiriet et al. (2019), but change three of these values. We reduce the mantle density from 3500 kg·m^{-3} to 3120 kg·m^{-3} to be consistent with Mercury's mass and the adopted density of the core. We keep the reference viscosity of the mantle at 1600 K of 10^{21} Pa·s for the baseline scenario and will vary the reference viscosity between 10^{20} Pa·s and 10^{22} Pa·s for other scenarios. Present-day surface concentrations of Th, U and K have been measured to be 220 ± 60 ppb, 90 ± 20 ppb and 1150 ± 220 ppm, respectively (Peplowski et al., 2011). Thiriet et al. (2019) and Tosi et al. (2013a) account for preferential partitioning of these elements into crustal minerals and adopted present-day concentrations of 50 ppb, 28 ppb and 400 ppm in Mercury's mantle. We multiply the present-day mantle abundances of Th, U and K used by Thiriet et al. (2019) and Tosi et al. (2013a) by a factor γ_{rad} between 0 and 3. Setting $\gamma_{rad} = 3$ represents scenarios in which the concentrations of radiogenic elements of the mantle are similar to those at Mercury's surface. For the baseline model of this paper, we set $\gamma_{rad} = 0.2$, corresponding to radiogenic elemental concentrations near the minimum of the range estimated for Mercury's mantle by Padovan et al. (2015).

We additionally investigate the occurrence and evolution of partial melt zones in the mantle and relate their evolution to the ancient large scale volcanism which produced Mercury's surface terrains of 3.7 *Ga* and older (Marchi et al., 2013; Denevi et al., 2013). Namur et al. (2016b) relate the composition of the youngest surface terrains of about 3.7 *Ga* to large scale volcanism with lavas that originate from partial melt in the mantle at temperatures between about 50 K and 100 K above the solidus curve of an EH enstatite chondrite (Namur et al., 2016b). We have listed the corresponding solidus in the caption of Table 1). We keep track of the mantle regions that are at least 75 K above the solidus, and define those regions as partial melt zone. We emphasise that the use of this solidus curve comes with limitations because mineral differentiation by mantle melting and subsequent melt migration affects the composition and increases the solidus over time (e.g. Maaløe, 2004; Morschhauser et al., 2011). Therefore, the duration of partial melt zones in the mantle determined in this paper is likely an upper limit.

3.2. Parameters of Mercury's core

The large Fe-rich core and the Fe-poor and S-rich surface composition of Mercury are indicative of a low redox state of the planet compared to the other terrestrial planets (Zolotov et al., 2013; Chabot et al., 2014; Namur et al., 2016a). At such reducing conditions, Si is the dominant light element to partition in Fe-rich metal during metal-silicate fractionation along with a few wt% of S and C (Chabot et al., 2014; Namur et al., 2016a; Steenstra and van Westrenen, 2020; Vander Kaaden et al., 2020). A core alloy in which Si is the dominant light element is in line with solidification starting at the center of the planet as is assumed in this study (Edmund et al., 2022), whereas solidification may start at the CMB and initiate Fe-snow if S is the dominant light element (Chen et al., 2008; Dumberry and Rivoldini, 2015). Following Thiriet et al. (2019), we use $\rho_c = 7200$ kg·m^{-3} and $R_c = 2010$ km. From the average density of the core, the composition of the core cannot be uniquely determined. For the baseline scenario, we assume that the core contains 7 wt% Si, and 1 wt% of S and C, which is a composition that agrees with the assumed core density (Knibbe et al., 2021) and with the above geochemical constraints. Moreover, unlike Si, light elements C and S have a strong depressing effect on the liquidus and partition more significantly into the liquid upon solidification and thus are expected to more strongly affect the thermal evolution and dynamo action in the core.

The adiabatic gradient (Eq. 22) depends on temperature, pressure, and on material properties of the core alloy. Since ρ_c is assumed constant, the pressure profile in the core is given by

$$P(r) = P_c + G\rho_c^2 \frac{2\pi}{3} \left(R_c^2 - r^2 \right) \tag{43}$$

with P_c the pressure at R_c. The radial profile of α_c for the Fe-7wt%Si-1wt%S-1wt%C alloy is computed along the pressure profile of Eq. (43) following Knibbe et al. (2021) and shown in Fig. C.10 (see Appendix C). The parameters τ_2 and τ_3 describing T_{ac} are determined by fitting Eq. (24) to the adiabatic gradient computed from the material parameters of Table 1 and α_c (Eq. 22) and are listed in Table 1.

In the pressure range of the core, $5-38$ GPa (Knibbe and van Westrenen, 2015), the liquidus depression relative to the melting curve of pure Fe due to the presence of light elements is about 15 - 40 K per wt %Si (Morard et al., 2011; Edmund et al., 2022), 50 - 90 K per wt%S (Fei et al., 1997, 2000; Morard et al., 2011; Pease and Li, 2022), and 100 - 175 K per wt%C (Fei and Brosh, 2014). Based on those values, we estimate the liquidus depression per average light element relative to pure Fe for Fe-7wt%Si-1wt%C-1wt%S liquid metal at between 28 - 63 K/wt%. We parameterise the core liquidus T_{cl} as a function of pressure and light element concentration in the liquid core X_{oc} as

$$T_{cl}(P) = T_{cl,1}\left(\frac{P - P_{cl,1}}{P_{cl,2}} + 1\right)^{\frac{1}{3}} + X_{oc}\frac{\mathrm{d}T_{cl}}{\mathrm{d}X}, \tag{44}$$

of which the first term with parameters $T_{cl,1}$, $P_{cl,1}$, and $P_{cl,2}$ (Table 1) stands for the liquidus of Fe (Morard et al., 2018), and $\mathrm{d}T_{cl}/\mathrm{d}X$ is the liquidus depression due to the presence of light elements per weight fraction. We set $\mathrm{d}T_{cl}/\mathrm{d}X$ at -50 K per wt% for our baseline scenario and set the initial value of X_{oc} at 9 wt%. We vary these parameters among other thermal evolution scenarios to assess how they affect the thermal evolution of the planet.

To large extent, the partitioning coefficient D_l^s determines the compositional buoyancy F_X and the associated entropy production E_X (Eq. 41). For Si, which is the dominant light element in the baseline scenario, D_l^s in Fe-rich binary Fe—Si alloys varies between 0.85 and 1 (Morard et al., 2014). The fractionation coefficient of S and C in Fe-rich binary Fe—S and Fe—C alloys is almost 0 (Fei et al., 1997, 2000) and between 0.3 and 0.5 (Fei and Brosh, 2014), respectively. The solid-liquid partitioning of these elements changes if ternary and quarterly systems are considered. For example, the small preferential partitioning of Si into Fe—Si liquid changes to preferential partitioning into solid metal if S or C are present (Deng et al., 2013; Tao and Fei, 2021; Sakai et al., 2023). Since accurate data for Fe alloys with multiple light elements are lacking, we set $D_l^s = 0.9$ for the baseline scenario but vary this parameter in other thermal evolution scenarios to assess how light element partitioning affects the thermal evolution.

The compositional expansion coefficient β_X (Eq. 37) varies considerably for Fe-Si-S-C alloys. In binary Fe—Si, β_X of Si is around 0.9 (Terasaki et al., 2019) whereas for S in Fe—S or Fe-10wt%Ni-S, β_X takes values between 1 and 2 (Knibbe et al., 2021; Terasaki et al., 2019). We fix β_X to 0.9 throughout this study because its effect on the thermal evolution is small if compared to the effect the D_l^s values considered in this study have.

The thermal conductivity (k_c) of liquid Fe is measured at ambient pressures and 1818 K by Nishi et al. (2003) to be 33 $\mathrm{W{\cdot}m^{-1}K^{-1}}$. Thermal conductivity increases with pressure and is extrapolated to about 43 $\mathrm{W{\cdot}m^{-1}K^{-1}}$ for liquid Fe for conditions at Mercury's CMB of about 1818 K and 5.5 GPa (Secco, 2017). Based on high-pressure electrical conductivity measurements on liquid Fe-rich alloys, a k_c of Fe-8.5 wt% Si at Mercury CMB conditions of about 32 $\mathrm{W{\cdot}m^{-1}K^{-1}}$ is inferred (Berrada et al., 2021). At conditions of Earth's CMB of 136 GPa and about 3000 K, the k_c of pure liquid Fe is calculated by first principles to be about 140 $\mathrm{W{\cdot}m^{-1}K^{-1}}$ (de Koker et al., 2012), whereas that of Fe-9 wt% Si liquid metal is deduced from electrical conductivity measurements to be around 100 - 110 $\mathrm{W{\cdot}m^{-1}K^{-1}}$ (Zhang et al., 2022). Linear interpolation between these estimated values of k_c at Mercury's CMB and Earth's CMB pressure conditions yield k_c of between 49 and 65 $\mathrm{W{\cdot}m^{-1}K^{-1}}$ at pressures of Mercury's center of about 36 GPa. Here we set k_c at 45 $\mathrm{W{\cdot}m^{-1}K^{-1}}$, which is between the estimates for k_c at Mercury's CMB and Mercury's center. We do not vary k_c among thermal evolution scenarios that we present in this paper.

The latent heat $L = T\Delta s$ of pure Fe is about 250 kJ/kg at the melting temperature of 1811 K (Desai, 1985). In this study, we set $L = 300$ kJ/kg, which is the value of L at the liquidus temperature of Mercury's center of the baseline scenario of 2197 K under the assumption that Δs is constant.

4. Results and discussion

4.1. The baseline scenario

In this section, we present the evolution in the baseline scenario. The mantle begins in a state of stagnant lid convection. Because the mantle cools, the viscosity increases, mantle convection weakens, and the layer between the thermal boundary layers in V_{cm} gradually gets thinner (Fig. 3). At 1.5 billion years, the thickness of the thermal boundary layers is about half the thickness of V_{cm} and the transition from a convective to a conductive state of the mantle begins. At about 3.8 Gyr, the thermal boundary layers touch and heat transport through the mantle occurs solely by conduction. A partial melt zone exists in V_{cm} early in the evolution and is located below the upper thermal boundary layer, in the convective region of the mantle. The zone that attains temperatures higher than 75 K above the solidus subsides at 0.8 Gyr, and temperatures become subsolidus everywhere in the mantle at 1.25 Gyr. This timing is consistent with the end of large-scale volcanism on Mercury at around 0.8 Gyr after planet formation (Denevi et al., 2013; Marchi et al., 2013) and with the temperatures of mantle source regions of the youngest surfaces (Namur et al., 2016b).

A thermally stratified region forms below the CMB almost immediately at the start of the evolution and grows to a thickness of about 1000 km after 2.2 Gyr when the inner core begins to solidify (Fig. 3). Due to the decrease of heat transport through the core, E_Φ decreases rapidly in the beginning of the evolution from several tens of MW/K to 1 MW/K at 700 Myr and below 0.1 MW/K at 2.2 Gyr (Fig. 3). The necessary condition for dynamo action, which is that $E_\Phi > 0$, is fulfilled throughout this time period. However, it is unclear whether such a minor amount of entropy production could be fully realised by viscous processes and no entropy production is available for ohmic dissipation. If a magnetic field would be generated by such minor forcing, it may be too weak to magnetize Mercury's crust at about 700 Myr as is suggested based on low-altitude magnetic field measurements (Johnson et al., 2015).

While the inner core grows to a present-day radius of 1340 km, latent heat and gravitational energy are released, which increases the heat flux through the liquid core and leads to a decrease of the thickness of V_{sc} to 473 km at present. As a result, E_Φ increases to about 10 MW/K over the final 2 Gyr of the evolution. Work done by thermal buoyancy is responsible for about 40% of this entropy production (E_T, associated with convective transport of heat), whereas the rest results from compositional buoyancy (E_X, associated with convective transport of light elements). E_{ac}, the entropy produced in V_{ac}, is two-thirds of E_Φ, whereas V_{ac} is only 30 % of the liquid core volume (Table 2) indicating that the local dissipation density ϕ is much larger in V_{ac} than in V_{sc}.

The transition from convective to conductive state of the mantle leads to a temporary dip in q_c at about 2.6 Gyr and a small and temporary decrease in E_Φ about half a billion years later (Fig. 3). The delay in the response of E_Φ is related to the conduction timescale of the thermally stratified layer in the liquid core, which is on the order of a billion years (Knibbe and Van Hoolst, 2021). Guerrero et al. (2021) present mantle convection simulations in which q_c is much larger than the 11 - 13 $\mathrm{mW/m^2}$ of our baseline scenario after convection has ended. The larger heat fluxes at the CMB are due to the larger mantle conductivity values they assumed between about 4 and 12 $\mathrm{W{\cdot}m^{-1}{\cdot}K^{-1}}$. We have set k_m at 4 $\mathrm{W{\cdot}m^{-1}{\cdot}K^{-1}}$, which is in agreement with the range of 2 - 5 $\mathrm{W{\cdot}m^{-1}{\cdot}K^{-1}}$ of silicate minerals at pressure and temperature conditions of Mercury's mantle of below 6 GPa and average temperature of between 1600 K - 1100 K (Fig. 2) (Tosi et al., 2013b; Zhang et al., 2019; Freitas et al., 2021).

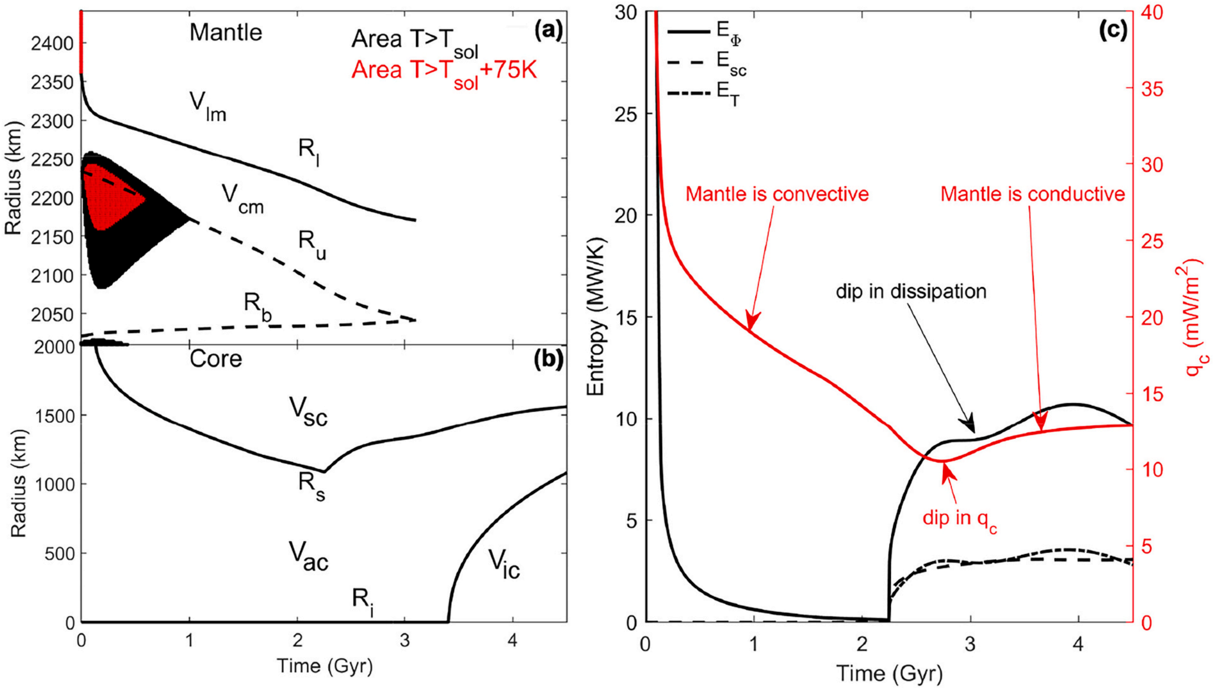

Fig. 3. This figure presents the baseline thermal evolution scenario (scenario 1 in Table 2). Panel (a) shows the evolution of V_{lm}, V_{cm}, and partial melt zones in the mantle. The black and red area denote the supersolidus region and the region where temperature is more than 75 degrees above the solidus, respectively. Interfaces of thermal boundary layers (R_u and R_b) are plotted as dashed lines. Panel (b) shows the evolution of R_i and R_s. Panel (c) shows the total production of entropy in the core that is available for ohmic dissipation (E_Φ, black solid, left axis), the entropy budget generated in the thermally stratified region (E_{sc}, black dashed) of which the complement is generated in the thermally convective region (E_{ac}), and the entropy budget that is generated by thermal buoyancy (E_T, dashed-dotted), of which the complement is generated by compositional buoyancy (E_X). The red line (right axis) shows the evolution of q_c. A dip in q_c at about 2.6 Gyr is related to the transition from a convective to a conductive state of the mantle, and induces a dip in E_Φ with a delay of about half a billion years. (For interpretation of the references to colour in this figure legend, the reader is referred to the web version of this article.)

4.2. Sensitivity to assumptions on the core's temperature profile

In this section, we compare the results of the baseline scenario with the adiabatic core model and the adiabatic inner core model introduced in Section 3. For the adiabatic core model, the evolution of T_c simplifies to

$$\frac{\mathrm{d}T_c}{\mathrm{d}t} = \frac{Q_L + Q_G + \rho_c H_c \frac{4\pi}{3} R_c^3 - q_c 4\pi R_c^2}{\epsilon(R_c)\rho_c c_c \frac{4\pi}{3} R_c^3}, \tag{45}$$

where $Q_G = Q_{G,ac} + Q_{G,cc}$ (Eqs. 38–39). We recall that assuming an adiabatic temperature profile in regions where the heat flux is sub-adiabatic implies the existence of a mechanism that transports heat downward. As a consequence, T_c is a few tens of degrees lower and the center of the planet is about 100 degrees warmer at present in the adiabatic core model (Fig. 4). The inner core therefore starts to solidify about 1 Gyr later and the present-day inner core is smaller by about 13 % of the core's volume. This also leads to a lower q_c and to an end of mantle convection about 800 million years earlier as compared to the baseline model. These differences are similar to those described in Knibbe and Van Hoolst (2021).

In the case of an adiabatic inner core the results are almost indistinguishable from the baseline scenario (not shown). The most significant difference is that the heat flux out of the inner core (q_i) is about 40 % smaller in the adiabatic inner core model, because assuming an adiabatic temperature profile in the thermally stratified inner core implicitly leads to downward heat transport and less heat from the inner core's interior reaches the inner core boundary. However, because of the smaller flux of heat toward the inner core boundary, a slightly larger growth rate of the inner core and of release of latent and gravitational heat is obtained that together largely compensate for the influence of the smaller q_i on the rest of the planet's thermal evolution.

We now describe differences in the entropy production available for ohmic dissipation E_Φ between the baseline model and the adiabatic core model. For the baseline model $E_\Phi = 9.6$ MW/K at present (Fig. 3) and consists of $E_T = 2.9$ MW/K, produced by F_T which is positive in V_{ac} and zero in V_{sc} and V_{ic} (Fig. 4f), and of $E_X = 6.7$ MW/K, produced by F_X in the liquid core (Fig. 4d). For the adiabatic core model, F_X is larger than in the baseline scenario because the inner core grows faster and generates $E_X = 9.3$ MW/K (Fig. 4d). More importantly, the downward convective flux of heat and associated negative F_T in thermally stratified regions of the adiabatic core model (Fig. 4e) consumes more entropy than what is generated by F_T in the thermally convective region of the core, such that $E_T = -14.1$ MW/K and $E_\Phi = -4.9$ MW/K. The computed entropy production in the adiabatic core model is 13.5 MW/K smaller than in the baseline model and below zero. In some studies, a negative E_Φ is interpreted as indication that dynamo action in the core cannot persist (Williams et al., 2007). But actually, a thermal evolution scenario in which E_Φ is negative, such as for the adiabatic core model, conflicts with the second law of thermodynamics and only implies that modelling assumptions are not valid.

In the adiabatic inner core model, the negative F_T in the inner core leads to E_Φ that is only about 3 MW/K lower than in the baseline scenario at present. Although $E_\Phi > 0$ in this model, if other model parameters are adopted that yield a larger present-day inner core, E_Φ can become negative (this is for example the case if we adopt an adiabat in the inner core for scenario 6 of Table 2). Because the influence of adopting an adiabat in the inner core on the thermal evolution is small but the influence on E_Φ can be substantial, some studies implement an adiabat in the thermally stratified inner core to simplify thermal evolution modelling but exclude the entropy consumption due to the associated downward heat transport in the inner core for computing E_Φ (Lister, 2003; Labrosse, 2015; Knibbe and van Westrenen, 2018).

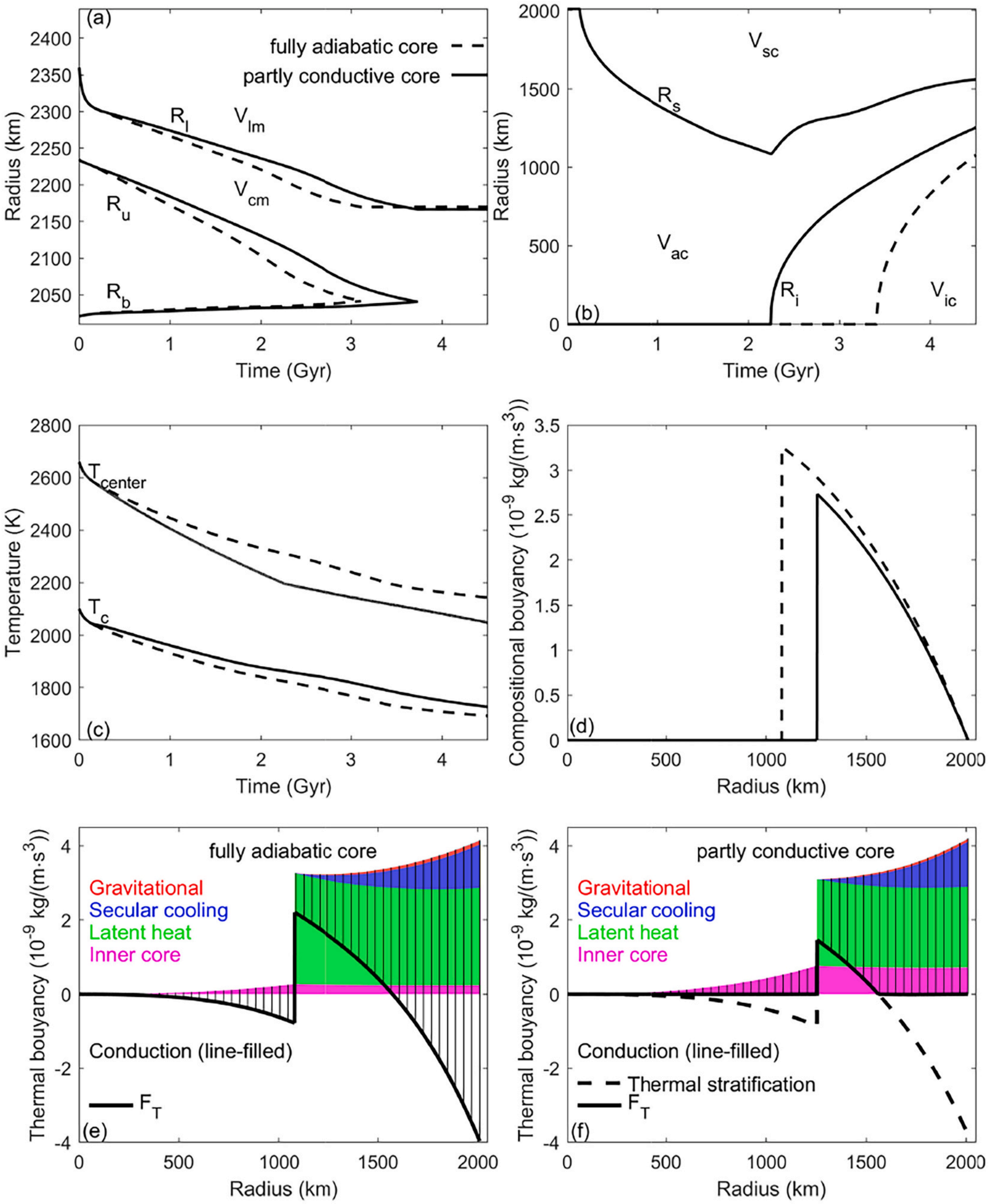

Fig. 4. Comparison of the baseline scenario (solid lines in panels (a)-(d), and panel (f)) and the adiabatic core model (dashed lines in panels (a)-(d), and panel (e)). (a) Evolution of lithospheric boundary (R_l) and of interfaces of the thermal boundary layers (R_u and R_b). (b) Inner core radius (R_i) and, for the baseline model, the evolution of V_{sc} and V_{ac}. (c) Temperature at the planet's center (T_{center}) and at the CMB (T_c). (d) Radial profile of F_X at present. Panels (e) and (f) show present-day profiles of F_T for the fully adiabatic and the partially conductive core models, respectively. Sources for F_T from the inner core due to secular cooling and for a negligible part by radiogenic decay (magenta), latent heat (green), secular cooling in the liquid core (blue), and gravitational heat (red) are distinguished. The contribution to F_T by radioactive decay in the liquid core is too small to be visible. The sink of F_T due to conductive heat transport is displayed as the area covered by vertical lines. In panel (f), the conductive sink is limited to the total of thermal buoyancy sources because the heat fluxes satisfy the conduction equation where the heat flux is subadiabatic, and the conservative thermally stratifying buoyancy force (which does no work in the baseline model because a conductive state is assumed) is plotted as dashed line. (For interpretation of the references to colour in this figure legend, the reader is referred to the web version of this article.)

However, some other thermal evolution studies do not exclude entropy consumption by the downward heat transport in the inner core and underestimate E_Φ potentially considerably (e.g. Greenwood et al., 2021a), unless there is a mechanism that transports the heat downward.

4.3. Sensitivity of thermal evolution and dynamo generation to parameters of Mercury's core

In this section, we examine the influence of the partitioning coefficient D_l^s, the core concentration of light elements X_c, and the effect of their amount on the core liquidus $\mathrm{d}T_{cl}/\mathrm{d}X$ on the thermal evolution and entropy production available for ohmic dissipation. These properties have a strong influence on the crystallisation and stratification in the core and on the relative contribution of compositional and thermal buoyancy to entropy production (see Fig. 5, scenarios 1 - 3 of Table 2). Other parameter values are identical to those of the baseline scenario.

Because the mantle's properties and adiabatic parameters of the core are fixed, the core liquidus T_{cl} determines when an inner core forms.

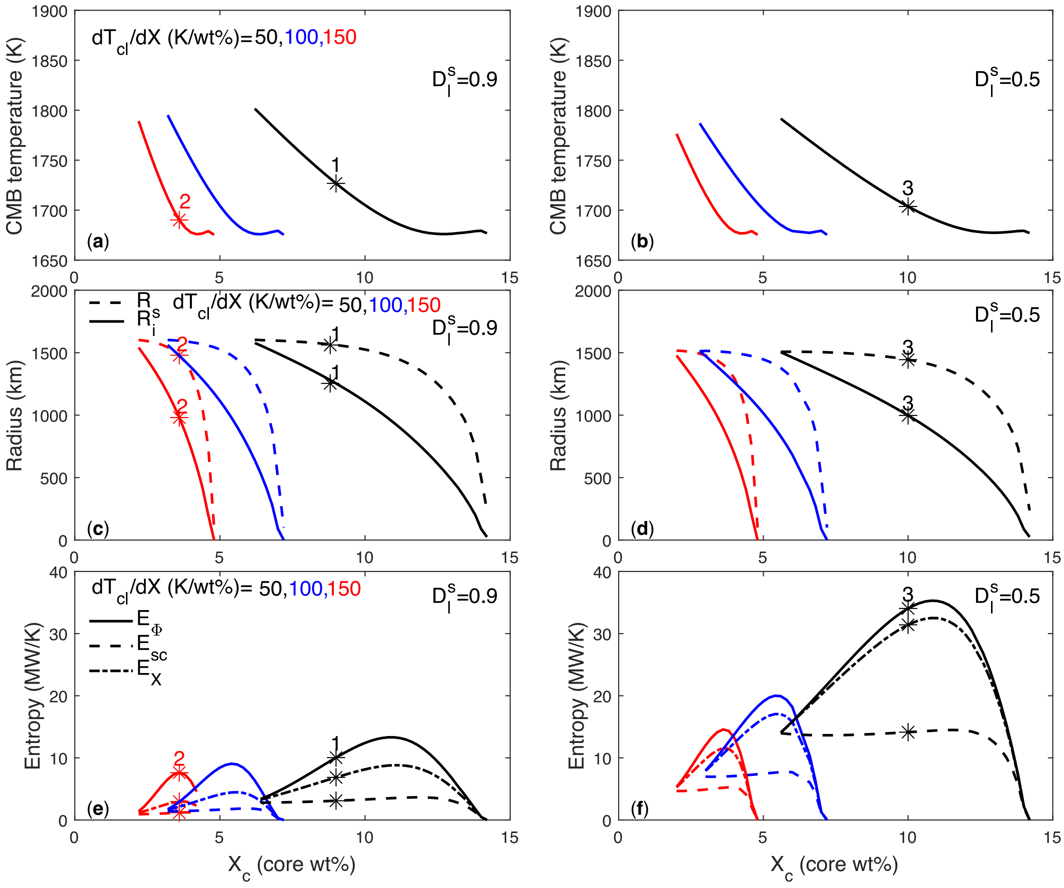

Fig. 5. Thermal evolution models with parameters of Table 1. Varied parameters among these scenarios are the light element concentration of the core (X_c, the X-axis), the liquidus depression due to light elements ($\mathrm{d}T_{cl}/\mathrm{d}X$) between 50 K/wt% (black), 100 K/wt% (blue), and 150 K/wt% (red), and the partitioning coefficient between solid and liquid (D_l^s) which is set to 0.9 for the left panels and 0.5 for the right panels. Panels (a) and (b) show the present-day T_c. Panels (c) and (d) show R_i (solid) and R_s (dashed). Panels (e) and (f) show E_Φ (solid), E_{sc} (dashed), and E_X (dashed-dotted). E_{ac} and E_T are the complements of E_{sc} and E_X relative to E_Φ, respectively. Only the scenarios with a present-day thermally convective layer ($R_s > R_i$) are shown. Table 2 lists some present-day characteristics of scenarios 1, 2, and 3, which are highlighted in this figure by snow-symbols. (For interpretation of the references to colour in this figure legend, the reader is referred to the web version of this article.)

Scenarios with $\mathrm{d}T_{cl}/\mathrm{d}X = 150$ K/wt%, 100 K/wt%, or 50 K/wt% yield a present-day thermally convective layer above the inner core and below a thermally stratified layer if 2 wt%$< X_c < 4.5$ wt%, 3 wt%$< X_c < 7$ wt%, or 6 wt%$< X_c < 14$ wt%, respectively (Fig. 5c,d). These ranges correspond to scenarios with a liquidus depression between about 300 K and 700 K. These scenarios are of particular interest since Mercury's present magnetic field is considered to be generated by a dynamo below a stably-stratified layer of the core (Christensen, 2006; Christensen and Wicht, 2008; Manglik et al., 2010; Takahashi et al., 2019). With increasing liquidus depression, the present-day inner core size decreases. Therefore, the release of latent and gravitational heat decreases and lower CMB temperatures are obtained (Fig. 5a-b). With liquidus depression approaching about 700 K, the core remains liquid and has become fully conductive with $E_\Phi = 0$ (Fig. 5c-f). With a decrease of the liquidus depression to about 300 K, the present-day inner core radius increases to about 1550 km and the CMB temperature increases by about 120 K relative to scenarios without an inner core as a result of the release of latent heat and gravitational energy (Fig. 5a-d). The liquid core is fully thermally stratified and E_Φ is exclusively produced by compositional buoyancy ($E_\Phi = E_{sc}$) (Fig. 5c-e). Our thermal evolution scenarios with a liquidus depression less than 300 K are inconsistent with the dynamo studies that reproduce the main characteristics of Mercury's magnetic field (e.g. Christensen, 2006; Christensen and Wicht, 2008; Manglik et al., 2010; Takahashi et al., 2019), which have thus far all assumed a thermally unstable lowermost layer in the liquid core.

The thermal evolution is not strongly affected by the partitioning coefficient D_l^s (Fig. 5a-d). Partitioning of light elements affects the thermal evolution largely through the release of gravitational heat (Q_G), which is small relative to the total heat production in the core (Table 2). The light element enrichment of the outer core also enhances the liquidus depression as the inner core grows, but also the effect on the thermal evolution is relatively small. Among the scenarios of Fig. 5c,d, the largest difference in the present-day inner core size using either $D_l^s = 0.5$ or 0.9 amounts to only 9 % of the core volume. Although the partitioning of light elements has a modest influence on the thermal evolution, it strongly affects the light element transport through the liquid core and consequently affects E_X and E_Φ. For example, thermal evolution scenarios with $D_l^s = 0.9$ yield a maximum E_Φ of about 13 MW/K of which E_X is about 60 %, whereas scenarios with $D_l^s = 0.5$ yield a maximum E_Φ of about 35 MW/K of which E_X is more than 90% (Fig. 5e,f). The large E_X in scenarios with large amounts of light element transport is the primary reason why Williams et al. (2007) obtain $E_\Phi > 0$ only if the concentration of S in the core is between 2 wt% and 8 wt%. Assuming such concentrations of S in the core, Williams et al. (2007) obtain a maximum for E_Φ at present of about 7 MW/K. In our thermal evolution model E_Φ is several times larger in similar thermal evolution scenarios because conductive heat transport in thermally stratified regions does not consume entropy, in contrast to the model of Williams et al. (2007), which assumes an adiabatic temperature profile in the whole core. In our thermal evolution scenarios with $D_l^s = 0.5$, E_Φ is dominantly generated by compositional buoyancy and between 40% and 100% is produced in the thermally stratified liquid layer (E_{sc}) (Fig. 5f).

In scenarios with $D_l^s = 0.9$, such as in the baseline scenario and scenario 2 (Fig. 5e, Table 2), at most 75 % of E_Φ is produced in V_{ac} at present. Using values for D_l^s closer to 1, the transport of light elements through the core will decrease and E_Φ will be increasingly dominated by E_T. Such results are more in line with our understanding of Mercury's present-day magnetic field. Dynamo simulations of Manglik et al. (2010) produce a magnetic field strength that agrees better with Mercury's magnetic field if the flux of light elements q_X is small. Simulations BU1–2 of Takahashi et al. (2019) successfully reproduce the main characteristics of Mercury's magnetic field only with negligible q_X in V_{sc}. Other characteristics of Takahashi et al. (2019)'s simulations BU1–2 are, however, more difficult to reproduce with our thermal evolution scenarios. Their background profiles (see their supplementary information) assume volumetric heating as the source of thermal buoyancy, whereas the thermally convective region in our thermal evolution models strongly relies on latent and inner core heat release at R_i. Additionally, at the bottom of the thermally stratified layer of their BU1–2 simulations, thermal instability sharply decreases with radius from its positive maximum to strongly negative, stratifying, values. The corresponding local sink of thermal buoyancy in the liquid core cannot be reproduced by our thermal evolution scenarios and is particularly difficult to combine with volumetric heating as the source for thermal buoyancy. Finally, the profile of compositional instability of their simulations BU1–2 is strong near R_i but decreases strongly with radius such that the thermally stratified region is only very weakly compositionally unstable. It is not clear what particular internal structure and light elements in the core will lead to a long-term evolution of the core with such a particular weak compositional stability in the upper thermally stratified layer while the release of light elements at R_i generates a strong compositional instability in the lower vigorously convective layer.

The magnetic field generation in a core with upper thermally stratified and compositionally buoyant layer atop a thermally and compositionally unstable layer is not well understood (e.g. Guervilly, 2022). But if models with substantial compositional buoyancy in the upper part of the liquid core can be ruled out (Manglik et al., 2010; Takahashi et al., 2019), the composition of the core can be constrained by the

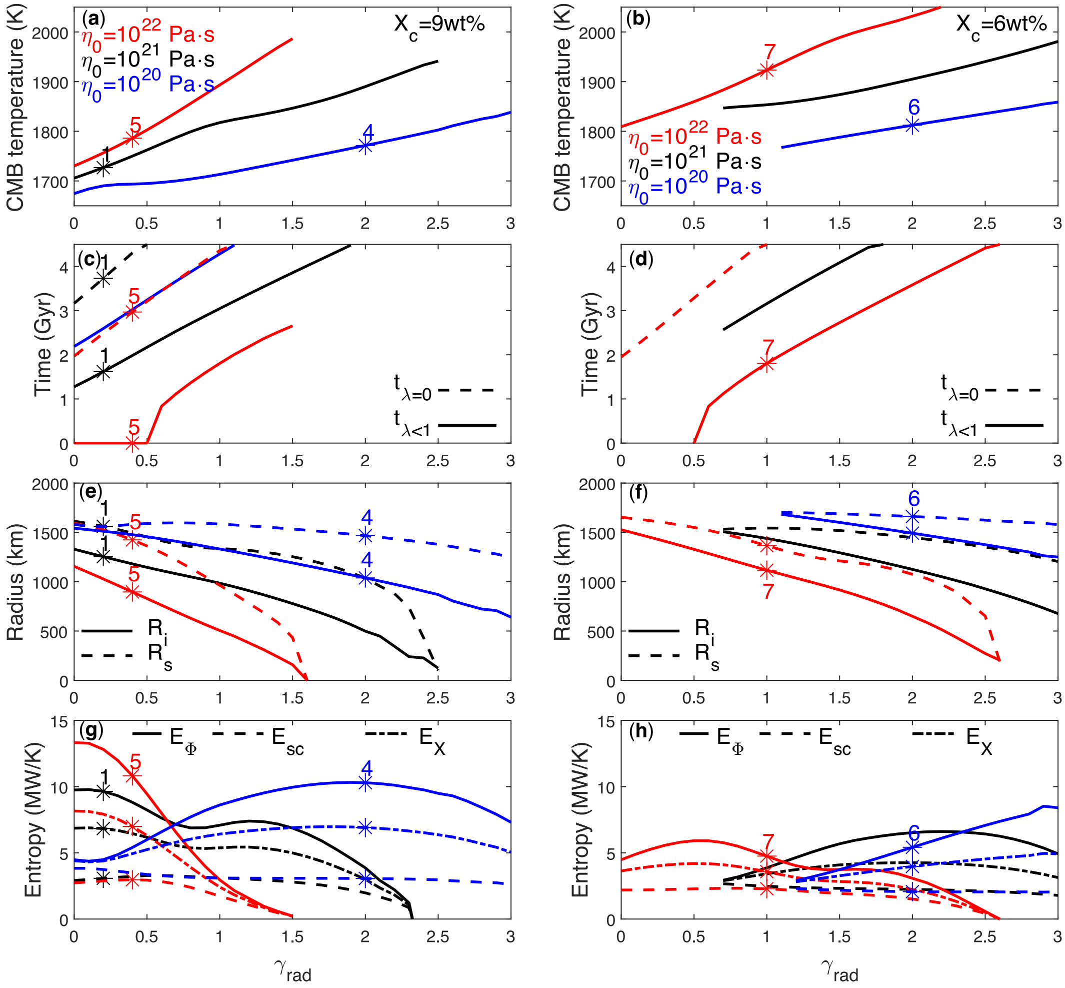

Fig. 6. Thermal evolution models with parameters of Table 1. Varied parameters among these scenarios are γ_{rad} which is proportional to the concentrations of radiogenic elements in the mantle (X-axis, $\gamma_{rad} = 3$ corresponds to mantle concentrations close to those observed at Mercury's surface and $\gamma_{rad} = 1$ to mantle concentrations used by Thiriet et al. (2019) and Tosi et al. (2013a)), the mantle's reference viscosity ($\eta_0 = 10^{22}$ Pa·s (red), 10^{21} Pa·s (black), or 10^{20} Pa·s (blue)), and core concentration of light element X_c, set to 9 wt% (left panels) or 6 wt% (right panels). Panels (a) and (b) show the present-day T_c. Panels (c) and (d) show the time when the transition from convective to conductive mantle begins ($t_{\lambda<1}$, solid) and ends ($t_{\lambda=0}$, dashed). In panel (c), the dashed blue line is absent because mantle convection persists in all scenarios with $\eta_0 = 10^{20}$ Pa·s. In panel (d), blue lines are absent because scenarios with $\eta_0 = 10^{20}$ Pa·s all yielded vigorously convective mantles up to the present. Panels (e) and (f) show R_i (solid) and R_s (dashed). Panels (g) and (h) show E_Φ (solid), E_{sc} (dashed), and E_X (dashed-dotted). E_{ac} and E_T are the complements of E_{sc} and E_X respectively, relative to E_Φ. Only the scenarios with a present-day thermally convective layer in the core are displayed. Table 2 lists some present-day characteristics of scenarios 4-7, which are highlighted in this figure by snow-symbols. (For interpretation of the references to colour in this figure legend, the reader is referred to the web version of this article.)

requirement that D^s_l is not much smaller than 1. This has implications for the composition of the core, since light elements S and C partition relatively strongly into the liquid whereas Si has a D^s_l only slightly below 1 (Section 3.2). Si should therefore be the dominant light element in the core, consistent with geochemical data. However, Si does not depress the Fe-liquidus as strongly as S and C, and a present-day thermally convective region in the liquid core is obtained only for thermal evolution scenarios with a liquidus depression larger than 300 K (Fig. 5c,d). Potentially, the increased partitioning of Si into solid during solidification of Fe-S-Si liquid metal (Tao and Fei, 2021) may lead to an effective D^s_l not much smaller than 1 for Fe-S-Si-C alloys while the addition of smaller amounts of S and C suffice to depress the liquidus by the required amount.

4.4. Sensitivity of thermal evolution and dynamo generation to parameters of Mercury's mantle

Because the thermal evolution of the mantle is dominantly controlled by its viscosity and radioactive heating, we present thermal evolution scenarios for different values of η_0 and γ_{rad} (Fig. 6, scenarios 4 - 7 of Table 2). We vary γ_{rad} between 0 and 3 and set η_0 at 10^{20} Pa·s, 10^{21} Pa·s, or 10^{22} Pa·s. The highest value for γ_{rad} is an upper limit, which corresponds to the mantle having about the same concentration of radioactive elements as observed at the surface. $\gamma_{rad} = 1$ is equivalent to assuming the mantle concentrations of radioactive elements used by Thiriet et al., 2019 and Tosi et al. (2013a). To examine also the influence of the core liquidus on these thermal evolution scenarios, we set X_c either to 9 wt%, as in the baseline scenario, or to 6 wt%. Other parameter values are as in the baseline scenario.

Higher concentrations of radioactive elements in the mantle lead to more internal heat production in the mantle and therefore to a higher temperature at the CMB and a longer duration of mantle convection (Fig. 6). The increase of CMB temperature with increase of γ_{rad} leads to a decrease of CMB heat flux, a faster growth of the thermally-stratified liquid layer, and slower growth of the inner core. A decrease of the viscosity in the mantle leads to a more efficient mantle convection with faster cooling of the core and mantle. Although decreasing viscosity and increasing concentrations of radioactive elements in the mantle have opposite effects on T_c, R_i and R_s, both prolong mantle convection.

Compared to the baseline scenario, increasing the mantle viscosity, concentration of radioactive elements, and light element concentration in the core, results in a smaller present-day inner core. If at present, an inner core has not formed, the entire core will be stratified with an E_Φ decreasing toward zero (Fig. 6e-h). With decreasing mantle viscosity, concentrations of radioactive elements, and light element concentrations in the core, the present-day inner core radius increases. When the present-day inner core radius increases to about 1500 km - 1700 km, the thermally convective layer vanishes and entropy is only produced in the thermally stratified layer E_{sc} by light element transport. The largest values of E_Φ are obtained for scenarios that yield present-day inner core radii between about 600 km and 1300 km. For those scenarios, the present-day mantle is either in a convective state with a low viscosity and high concentrations of radiogenic elements, or in a conductive state with a high viscosity and low concentrations of radiogenic elements. Hence, a convective mantle is not a necessary condition for obtaining $E_\Phi > 0$, in contrast to the conclusion of Williams et al. (2007).

5. Conclusions

We have coupled the mantle and core in a planetary thermal evolution model for Mercury in which both the mantle and core can undergo a transition from a convective to a conductive state. We use this model to investigate how the coupling of the core and mantle affect the thermal evolution of the planet and the generation of the magnetic field in the core. In particular, we assess which parameter choices lead to thermal evolution scenarios that yield a thermally convective layer in the liquid core below a thick thermally stratified layer, as such a configuration is thought to be consistent with main aspects of the observed magnetic field (Christensen, 2006).

Plausible thermal evolution scenarios that satisfy minimum conditions for present-day dynamo action in a thermally convective layer below a thermally stratified layer in the liquid core are possible with both a present-day convective mantle and a present-day conductive mantle. A convective mantle is thus not a necessary condition for present-day dynamo action in Mercury's core (Williams et al., 2007) nor is a present-day conductive mantle with high thermal conductivity (Guerrero et al., 2021) required. By assuming relatively low concentrations of radiogenic elements in the mantle, a relatively viscous mantle, and/or assuming a low core liquidus, our thermal evolution model can produce a present-day state with entropy production in the core available for dynamo action with a conductive mantle and with relatively low core temperatures. By assuming relatively high concentrations of radiogenic elements, a lower viscosity for the mantle, and assuming a higher liquidus of the core, the thermal evolution model can produce a present-day state of Mercury with entropy production in the core available for dynamo action with a convective mantle and with relatively high core temperatures.

We have clarified how adopting either an adiabatic or conductive temperature profile in regions of the core where the heat flux is subadiabatic affects entropy production available for dynamo action. If an adiabatic temperature profile is assumed where the heat flux is subadiabatic, the existence of a mechanism that transports heat downward is implied. Downward heat transport consumes power that would otherwise be available for dynamo action. If insufficient power is available to transport heat downwards, the simulated thermal evolution is at odds with the second law of thermodynamics. If heat transfer in thermally stratified regions is described by conduction (Labrosse et al., 1997; Knibbe and van Westrenen, 2018), the computed power available for dissipative processes is nonnegative and the second law of thermodynamics is implicitly satisfied. Additionally, the rate of entropy production available for ohmic dissipation is larger and minimum conditions for dynamo action in Mercury's core are more easily met.

The results of this paper show that a significant thermally convective layer deep in the core can persist until today if the core liquidus is several hundred K below that of pure Fe. Such a liquidus depression can be obtained by assuming a significant amount of light elements in the core. Scenarios with a liquidus depression of 300 K require relatively high present-day temperatures in the core for a substantial thermally convective region in the core to persist until the present and for mantle temperatures to become subsolidus after large scale volcanism (Denevi et al., 2013; Marchi et al., 2013). For those scenarios, the mantle's temperature at 0.8 Gyr is above the temperatures that are estimated for mantle source regions of volcanic lava that produced Mercury's youngest surfaces (Namur et al., 2016b). With a core liquidus depression of about 450 K, thermal evolution scenarios can yield mantle temperatures that are in line with surface observations (Namur et al., 2016b) and with a present-day thermally convective region that may produce a dynamo below a thermally stratified region in the core.

If the preferential partitioning of a light element into the liquid core alloy during inner-core solidification is strong, the resulting flux of the light element through the upper thermally stratified layer is at odds with dynamo models that best explain the observed magnetic field (Manglik et al., 2010; Takahashi et al., 2019). Thermal evolution scenarios from this study indicate that a partitioning coefficient slightly below unity creates conditions suitable for past and present-day dynamo operation below a thick stable layer. Although Si partitions almost equally between solid and liquid iron, its effect on the liquidus is too small to sustain dynamo action up to present-day. The addition of smaller fractions of S and/or C to Fe—Si is sufficient to depress the liquidus by the required amount, while at the same time the combined effect of these light elements results in a large enough effective partition coefficient

(Tao and Fei, 2021).

The thermal evolution scenarios in this paper have assumed a thermal conductivity of the core k_c of 45 W·m^{-1}K^{-1} and we assumed fixed parameters for describing the adiabat. If the core has a larger k_c, more heat is transported through the core by conduction and less by convection. Therefore, a larger k_c relative to the value used in this study results in a thinner thermally convective liquid region in the core and lower entropy production by thermal buoyancy. A smaller k_c would have the opposite effect. Furthermore, a steeper adiabat of the core would result in a larger maximum conductive heat flux in the core and a thinner thermally convective liquid region and decreased entropy production by thermal buoyancy deep in the liquid core whereas a smaller adiabatic gradient would have the opposite effect.

Unlike the results in our study that require non-equal partitioning of light elements between the solid and liquid core to explain a present-day dynamo, Davies et al. (2024) find that Mercury's dynamo can operate in a Fe—Si core if equal partitioning of Si is assumed. Three different assumptions about the thermodynamic and transport properties of Mercury's core with respect to our study result in differences in generated entropy and interior structure. Two of those differences, a significantly higher latent heat (500 kJ/kg versus 300 kJ/kg) and a composition, pressure, and temperature dependent thermal conductivity that is significantly below the value we assumed at upper core pressures, make a dynamo more likely. But the main reason why they find that a dynamo is possible for a Fe—Si core is their different parameterisation of the core liquidus. Davies et al. (2024) assume that the core liquidus of Fe—Si is higher, decreases slower with Si than our generic light element, and neglect the existence of the Fe-FeSi eutectic. Experimental results (Ozawa et al., 2016; Edmund et al., 2022) show that the eutectic concentration decreases with increasing pressure and is below 10 wt% at 40 GPa (Mercury's center core pressure). Above the eutectic, the liquidus increases with Si. If the core temperature drops below the liquidus, a likely buoyant solid will crystallize (Edmund et al., 2022). It is not known if the gravitational power generated by up-floating solid can help to drive a long-lived dynamo and, at the same time, not destabilize the upper core stable layer. The models presented in Davies et al. (2024) that allow for a past and present-day dynamo have Si concentrations likely above the eutectic at core center pressures and are built on the premise of bottom-up inner core nucleation.

Our results lean heavily on not well-known thermodynamic and transport properties of core forming materials. In particular the combined effect of light elements on thermal conductivity and phase stability is not well understood and mostly deduced from results obtained from binary alloys. Consequently, future experimental data are expected to refine and potentially alter some of the conclusion drawn in this study. Additionally, new measurements that will be obtained by BepiColombo will improve constraints on Mercury's interior structure and thermal state and are expected to inform about the radius of the inner core (Genova et al., 2021). Together with new experimental findings, these data will increase our understanding of the core's thermal evolution and the magnetic field generation.

CRediT authorship contribution statement

Jurrien Sebastiaan Knibbe: Writing – original draft, Visualization, Validation, Software, Methodology, Investigation, Formal analysis, Conceptualization. **Attilio Rivoldini:** Writing – review & editing, Writing – original draft, Investigation, Conceptualization. **Yue Zhao:** Software, Investigation, Formal analysis. **Tim Van Hoolst:** Writing – review & editing, Supervision, Software, Resources, Project administration, Methodology, Funding acquisition.

Declaration of competing interest

The authors declare that they have no known competing financial interests or personal relationships that could have appeared to influence the work reported in this paper.

Acknowledgements

This work was financially supported by the Belgian PRODEX program managed by the European Space Agency in collaboration with the Belgian Federal Science Policy Office, contract numbers PEA4000140326 and 4000129360 Planet Interior of the European Space Agency. We also acknowledge support from the programme BRAIN-be 2.0 (B2/191/P1/STEM). This publication is part of the project Mercury from MESSENGER to BepiColombo with file number ENW.GO.002.006 of the research programme User Support Planetary Science which is (partly) financed by the Dutch Research Council (NWO). The code that is developed for this study and used to produce the results in this paper is freely available at an online repository (Knibbe, 2024).

Appendix A. Parameterisation of thermal boundary layers in the mantle

In this appendix, we first reiterate the parameterisation of the thermal boundary layers from Thiriet et al. (2019). Subsequently, we list the expressions of other variables of the mantle's temperature profile and the associated heat fluxes.

The viscosity in the upper thermal boundary layer is related to T_m as

$$\eta_u = \eta_{ref} exp\left[\frac{A}{\mathcal{R}}\left(\frac{1}{T_m} - \frac{1}{T_{ref}}\right)\right], \tag{A.1}$$

with $\mathcal{R}$ the ideal gas constant and A an activation constant. The viscosity in the bottom thermal boundary layer is related to the temperature in that boundary layer as

$$\eta_b = \eta_{ref} exp\left[\frac{A}{\mathcal{R}}\left(\frac{2}{T_m + T_c} - \frac{1}{T_{ref}}\right)\right]. \tag{A.2}$$

Separate Rayleigh numbers are defined for the upper thermal boundary layer

$$Ra_u = \frac{\alpha_m \rho_m g_m (T_c - T_l)(R_l - R_c)^3}{\kappa \eta_u} \tag{A.3}$$

and for the bottom thermal boundary layer

$$Ra_b = \frac{\alpha_m \rho_m g_m (T_c - T_l)(R_l - R_c)^3}{\kappa \eta_b}. \tag{A.4}$$

The internal Rayleigh number of the mantle is

$$Ra_i = \frac{\alpha_m \rho_m g_m \left(T_c - T_p\right)\left(R_p - R_c\right)^3}{\kappa \eta_b}, \tag{A.5}$$

and the critical Rayleigh number is

$$Ra_{crit} = 0.28 Ra_i^{0.21}. \tag{A.6}$$

The thicknesses of the thermal boundary layers are described in terms of the above Rayleigh numbers as

$$\delta_b = (R_l - R_c)\left(\frac{Ra_{crit}}{Ra_b}\right)^{\beta^b} \tag{A.7}$$

and

$$\delta_u = (R_l - R_c)\left(\frac{Ra_{crit}}{Ra_u}\right)^{\beta^u}. \tag{A.8}$$

The temperature difference across the upper thermal boundary layer is Enova as

$$T_m - T_l = \frac{a_{rh} \mathcal{R} T_m^2}{A}, \tag{A.9}$$

where a_{rh} is a scaling parameter.

The energy that corresponds to the temperature profile $T_{cm,conv}$ of Eq. (15) is

$$\begin{aligned} \mathscr{E}_{cm} = \rho_m c_m &\left[T_m \frac{4\pi}{3}\left(R_l^3 - R_c^3\right) - \frac{T_m - T_l}{\delta_u}\left(\pi\left(R_l^4 - R_u^4\right) - \frac{4\pi}{3} R_u \left(R_l^3 - R_u^3\right)\right)\right] \\ &+ \rho_m c_m \left[\frac{T_c - T_m}{\delta_b}\left(\frac{4\pi}{3} R_b \left(R_b^3 - R_c^3\right) - \pi\left(R_b^4 - R_c^4\right)\right)\right] \end{aligned} \tag{A.10}$$

The heat fluxes in and out of V_{cm} that are associated to $T_{cm,conv}$ are given by

$$q_{c,\mathrm{conv}} = -k_m \frac{T_m - T_c}{\delta_b} \text{ and } q_{l,conv} = -k_m \frac{T_l - T_m}{\delta_u} \tag{A.11}$$

with k_m the thermal conductivity of the mantle.

The time-dependent parameters S_{cm}, A_{cm}, and B_{cm} of $T_{cm,cond}$ (Eq. 18) are solved using temperature boundary conditions T_l and T_c and by equating E_{cm} that corresponds to this temperature profile through Eq. (3). We obtain

$$S_{cm} = \frac{\mathscr{E}_{cm} - \rho_m c_m \left[\frac{4\pi}{3}\left(R_l^3 - R_c^3\right)\left(T_c - \frac{R_l(T_l - T_c)}{R_c - R_l}\right) + \frac{2\pi R_l \left(R_l^2 - R_c^2\right)(T_l - T_c)}{1 - \frac{R_l}{R_c}}\right]}{\rho_m c_m \left[\frac{4\pi}{6k_m}\left(\frac{R_l^3 - R_c^3}{3}\left(R_c^2 + \frac{R_l^3 - R_l R_c^2}{R_l - R_c}\right)\right) + \frac{R_l^2 - R_c^2}{2} \frac{R_l^3 - R_l R_c^2}{1 - \frac{R_l}{R_c}} - \frac{R_l^5 - R_c^c}{5}\right]} \tag{A.12}$$

$$A_{cm} = \frac{R_l(T_l - T_c) + \frac{S_{cm}}{6k_m}\left(R_l^3 - R_l R_c^2\right)}{1 - \frac{R_l}{R_c}}, \tag{A.13}$$

and

$$B_{cm} = T_c + \frac{S_{cm} R_c^2}{6k_m} - \frac{A_{cm}}{R_c}. \tag{A.14}$$

The conductive heat fluxes in and out of V_{cm} that correspond to $T_{cm,cond}$ are related to the local thermal gradients as $-k_m \nabla T(R_c)$ and $-k_m \nabla T(R_l)$, respectively, and expressed as

$$q_{c,\mathrm{cond}} = -k_m\left(-\frac{S_{cm}R_c}{6k_m} - \frac{A_{cm}}{R_c^2}\right) \text{ and } q_{l,\mathrm{cond}} = -k_m\left(-\frac{S_{cm}R_c}{6k_m} - \frac{A_{cm}}{R_l^2}\right). \tag{A.15}$$

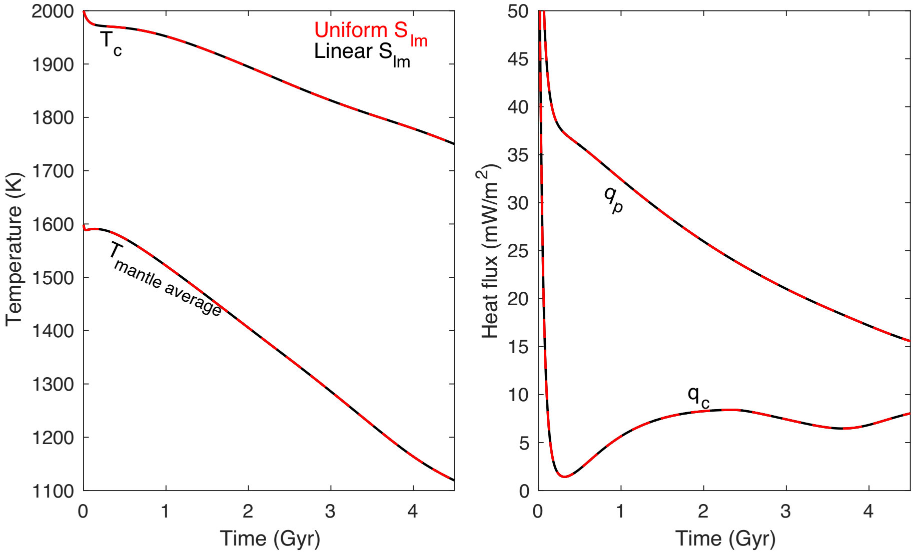

Fig. A.7. Computed thermal evolution in which we either adopt a uniform distribution of S_{lm} over the lithosphere (dashed red lines), or vary S_{lm} linearly with depth (solid black line which is plotted below the red dashed line). (For interpretation of the references to colour in this figure legend, the reader is referred to the web version of this article.)

The time-dependent parameters s_{lm}, A_{lm} and B_{lm} of Eq. (21) are solved from temperature boundary conditions $T_{lm}(R_p) = T_p$ and $T_{lm}(R_l) = T_l$ and flux boundary condition $-k_m\nabla T_{lm}(R_l) = q_l$

$$s_{lm} = -\frac{T_l - T_p - \frac{q_l R_l}{k_m R_p}(R_p - R_l) - \frac{\rho_m H_m}{6k_m R_p}\left(R_p^2 - R_l^2 - 2\frac{R_l^2}{R_p}(R_p - R_l)\right)}{\frac{3R_l^2(R_p - R_l)}{6k_m}\left(1 - \frac{R_l}{R_p}\right)}, \tag{A.16}$$

$$A_{lm} = R_l^2\left(\frac{3s_{lm}R_l^2}{6k_m} + \frac{q_l}{k_m} - \frac{R_l}{3k_m}(R_p s_{lm} + \rho_m H_m)\right), \tag{A.17}$$

and

$$B_{lm} = T_p - \frac{A_{lm}}{R_p} + \rho_m H_m \frac{R_p^2}{6k_m}. \tag{A.18}$$

The thermal energy that corresponds to T_{lm} is given by (Eq. 3)

$$\begin{aligned} \mathscr{E}_{lm} &= \rho_m c_m\left(A_{lm}2\pi\left(R_p^2 - R_l^2\right) + B_{lm}\frac{4\pi}{3}\left(R_p^3 - R_l^3\right)\right) \\ &+ \rho_m c_m\left(-(s_{lm}R_p + \rho_m H_m)\frac{4\pi}{30k_m}\left(R_p^5 - R_l^5\right) + s_{lm}\frac{4\pi}{36k_m}\left(R_p^6 - R_l^6\right)\right). \end{aligned} \tag{A.19}$$

The surface heat flux that is radiated to space is

$$q_p = -k_m\left(\frac{3s_{lm}R_p^2 - 2R_p(s_{lm}R_p + \rho_m H_m)}{6k_m} - \frac{A_{lm}}{R_p^2}\right). \tag{A.20}$$

The abundance of radioactive species ^{232}Th, ^{40}K, ^{235}U, ^{238}U decreases exponentially with time, with a lifetime that varies per radiogenic constituent. We accordingly describe the radiogenic production of heat per unit of mass by

$$H_m = \sum_{i\in\{^{232}\mathrm{Th},^{40}\mathrm{K},^{235}\mathrm{U},^{238}\mathrm{U}\}} X_{i,0}I_i e^{-\frac{1}{\tau_i}}, \tag{A.21}$$

where τ_i is the average lifetime of radiogenic element $i \in \{^{232}\mathrm{Th},^{40}\mathrm{K},^{235}\mathrm{U},^{238}\mathrm{U}\}$, I_i is the energy release of radiogenic species i per unit of mass decay, and $X_{i,0}$ is the concentration in the mantle of radiogenic constituent i at the beginning of the evolution (at which we set $t = 0$). The initial concentration of radiogenic elements can be written in terms of present-day concentrations by

$$X_{i,0} = X_i e^{\frac{\Delta t}{\tau_i}}, \tag{A.22}$$

where X_i is the present-day abundance of radiogenic element i in the mantle and Δt is the timespan between present-day and the start of the thermal evolution scenario (we set $t = 4.5$ Gyr at present day, such that $\Delta t = 4.5$ Gyr). The internal heat production in V_{cm} and V_{lm} are given by

$$Q_{cm} = \rho_m H_m \frac{4\pi}{3}\left(R_l^3 - R_c^3\right) \tag{A.23}$$

and

$$Q_{lm} = \rho_m H_m \frac{4\pi}{3}\left(R_p^3 - R_l^3\right). \tag{A.24}$$

To test the importance of implementing that S_{lm} varies linearly with depth as in Eq. (21), we compared the obtained thermal evolution with a scenario in which we adopt a uniformly distributed S_{lm}. The results, shown in Fig. A.7, indicate that the differences in adopting either a uniform of linear variation with depth of S_{lm} has a very minor effect on the obtained thermal evolution. The difference is on the order of 0.01 K on T_c and on the average mantle temperature and on the order of 10^{-4} mW·m^{-2} on q_c and q_p.

Appendix B. Calibration and discussion of parameters that describe the mantle's thermal behaviour

Our thermal evolution model of the mantle closely follows that of Thiriet et al. (2019), but differs from it on four aspects. Firstly, we have assumed that heat flux is continuous at R_l and we determine the growth rate of V_{lm} by enforcing strict energy balance of V_{lm} and V_{cm}. Thiriet et al. (2019) and many other studies before (Schubert et al., 1979; Stevenson et al., 1983; Morschhauser et al., 2011; Grott et al., 2011) adopt a discontinuity of heat flux at R_l, which is used with a local energy balance principle to determine the growth rate of the lithosphere. Secondly, we have considered the entire temperature profile T_{cm}, including thermal boundary layers, in the energy balance considerations of V_{cm} whereas Thiriet et al. (2019) and the cited other studies assume for heat balance considerations that T_m is the average temperature in V_{cm}. However, T_m is not equal to the average temperature of V_{cm} and the time variation of T_m is not necessarily equal to the time variation of the average temperature in V_{cm}. Particularly when thermal boundary layers grow to a substantial size, which is the case in thermal evolution models where convection strongly weakens or ends during the considered evolution, this practise introduces an error. Thirdly, we parameterise T_{lm} by considering that energy is balanced, by assuming that surface temperature is constant and the cooling rate varies with depth. To this end, we adopted a solution of the conduction equation in which secular cooling varies linearly with depth (Eq. 20). This approach is a simplification as compared to solving the conduction equation numerically, as is done by Thiriet et al. (2019). Finally, we have parameterised a smooth transition from convective state of the mantle to a conductive state of the mantle which has not been considered previously.

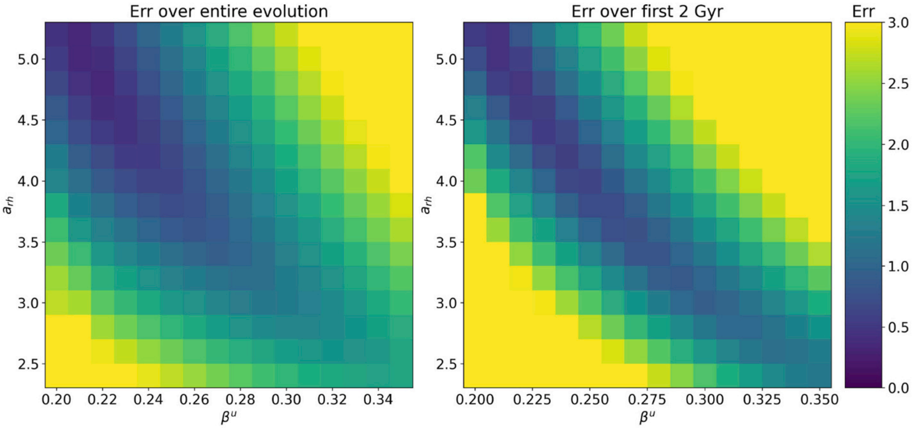

Fig. B.8. Computed error of fit (Eq. B.2) for comparing the parameterised thermal evolution model with the 2D thermal evolution mantle convection simulation. The first 200 million years of the thermal evolution are excluded. (left) Error of fit computed over the entire evolution. (right) Error of fit computed considering only the first two billion years of the thermal evolution. Errors above 3.0 are truncated to 3.0.

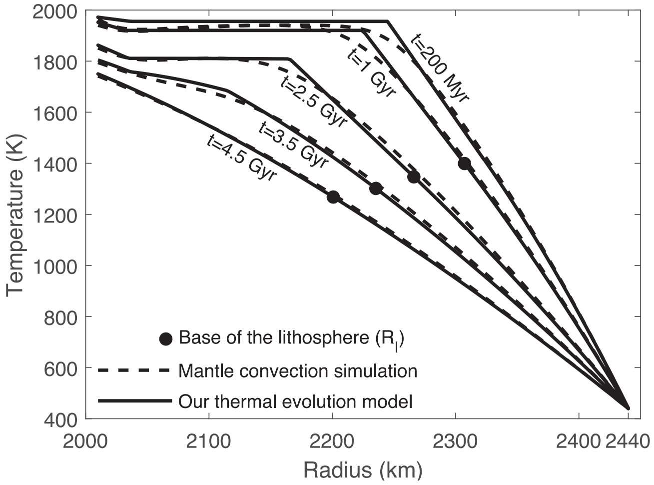

Fig. B.9. Temperature profiles of the mantle at $t = 200$ Myr, $t = 1$ Gyr, $t = 2.5$ Gyr, $t = 3.5$ Gyr, and $t = 4.5$ Gyr produced by the mantle convection simulation using the Gaia code (dashed lines) and produced by out thermal evolution model using parameters $a_{rh} = 2.1$ and $\beta^u = 5.1$ (solid lines).

For the purpose of comparison with Thiriet et al. (2019), in this appendix we treat the core as a thermal capacitor without heat sources

$$\frac{\mathrm{d}T_c}{\mathrm{d}t} = -\frac{q_c 4\pi R_c^2}{\rho_c c_c \frac{4\pi}{3} R_c^3}, \tag{B.1}$$

with ρ_c and c_c the density and heat capacity of the core. Fig. 2 shows the main heat balance of the mantle; the average mantle temperature and the heat fluxes in (q_c) and out of the mantle (q_p) save for production of radiogenic decay which is identical among the compared scenarios. Only the first two billion years of evolution is computed by Thiriet et al. (2019) and available for direct comparison, because mantle convection becomes weak and the parameterised model of mantle convection inappropriate. Using identical parameters as in Thiriet et al. (2019) our thermal evolution model yields q_c at 2 billion years of 6.8 mW·m^{-2}, which is about 1 mW·m^{-2} lower than that of Thiriet et al. (2019) (Fig. 2). For this reason, the mantle cools slightly faster in our thermal evolution model as compared to that of Thiriet et al. (2019) (Fig. 2). We have tested whether this difference in the evolution is related to our parameterised conductive heat transfer through the lithosphere as opposed to solving the conduction equation numerically. But the magnitude of the error that results from our simplified conductive heat transfer is much smaller than this difference. Neither can the transition from convective to conductive state of the mantle be the cause of this difference because this transition has not yet begun in the modelled period. The minor difference between Thiriet et al. (2019) ‘s and our model is likely related to differences in (dis)continuity assumptions of the heat flux at R_l and by the different heat balance considerations of V_{cm} that are described above.

Although the differences between our thermal evolution model of the mantle and that of Thiriet et al. (2019) is minor - our CMB heat flux is about 1 mW·m^{-2} lower - this difference does motivate us to re-calibrate parameters a_{rh} and β^u which largely control the mantle’s thermal behaviour. As a benchmark for the thermal behaviour of Mercury’s mantle, we perform a 2D mantle convection simulation with the Gaia code in 2D spherical annulus geometry (Hüttig et al., 2013; Fleury et al., 2024) using identical parameter values as in the simulation of Thiriet et al. (2019), which are also listed in Table 1. We vary a_{rh} and β^u of the parameterised model and compute an ‘error of fit’ as a weighed sum of differences between the surface heat fluxes, CMB heat fluxes and average mantle temperature, between our parameterised thermal evolution model and the simulated evolution as

$$Err = \frac{t}{t_{end} - t_0}\int_{t_0}^{t_{end}} \frac{\left|q_c - q_{c,sim}\right|}{3\mathrm{mW{\cdot}m^{-2}}} + \frac{\left|q_p - q_{p,sim}\right|}{3\mathrm{mW{\cdot}m^{-2}}} + \frac{\left|\overline{T} - \overline{T}_{sim}\right|}{20\mathrm{K}}\,\mathrm{d}t, \tag{B.2}$$

where $\overline{T}$ is the volume average temperature of the mantle, variables subscripted by ‘sim’ correspond to the simulated evolution, other variables correspond to the parameterised evolution, and t_0 and t_{end} correspond to the start and end of the time period over which the error is calculated. We set $t_0 = 200$ Myr and set t_{end} either at 2 Gyr or 4.5 Gyr. The weights that are used in Eq. (B.2) are the same as those adopted in Thiriet et al. (2019) and make sure that the differences of each of the three considered variables contribute a similar magnitude to the calculated error.

The results are shown in Fig. B.8. Largest errors are obtained if we calculate the error exclusively over the first 2 Gyr where the mantle is in convective state, because conduction that dominates the latest half of the evolution is accurately modelled both in the simulation and in the parameterised thermal evolution model, such that the evolutionary trajectories converge during that time-period. The lowest errors are obtained with $a_{rh} = 5.1$ and $\beta^u = 2.1$, and a comparison between the thermal evolution of the mantle convection simulation and our thermal evolution model with these parameter values is shown in Fig. B.9 and Fig. 2). We remark that the CMB heat flux of our 2D simulation is slightly larger than that of Thiriet et al. (2019)’s model (Fig. 2). It is possible that the spherical annulus geometry of our numerical simulation causes a slight overestimation of the CMB heat flux (Thiriet et al. (2019)). We note that $a_{rh} = 4.0$ and $\beta^u = 0.25$ should be used with our thermal evolution model to closely approximate the thermal evolution of Mercury simulated by Thiriet et al. (2019).

Convective flow strongly weakens shortly after 2 billion years in the simulated 2D mantle convection simulation which leads to a decrease of the CMB heat flux between 2.0 and 3.9 billion years (Fig. 2). The CMB heat flux increases at about 3.9 billion years in this thermal evolution scenario while conductive heat transfer becomes dominant (Guerrero et al., 2021). The transition from convective state to conductive state is modelled in our parameterised thermal evolution models by x_1 and x_2 (Eq. 19). We best approximate the simulated thermal evolution by invoking a relatively rapid transition from convective to conductive heat transfer that starts when the thermal boundary layers occupy almost half of the thickness of the convective mantle, which occurs at about 2 billion years in this thermal evolution scenario. Accordingly, we set $x_1 = 0.53$ and $x_2 = 2$ (Fig. 2).

Appendix C. Expressions for the core's temperature profile

In this appendix, we list expressions for variables in Section 2.3. Because the heat flux vanishes at the planet's center, T_{ic} simplifies to

$$T_{ic}(r) = -\frac{S_{ic}}{6k_c}r^2 + B_{ic}, \tag{C.1}$$

The parameters in Eq. (C.1) are given by

$$B_{ic} = \frac{5\mathscr{E}_{ic} - \rho_c c_c 4\pi T_i R_i^3}{\rho_c c_c \frac{8\pi}{3} R_i^3}, \tag{C.2}$$

and

$$S_{ic} = 6k_c \frac{B_{ic} - T_i}{R_i^2}. \tag{C.3}$$

The heat flux from V_{ic} to V_{ac} is

$$q_i = S_i \frac{R_i}{3}. \tag{C.4}$$

Since temperature and heat flux at R_s are continuous, q_s can be expressed as

$$q_s = -k_c \frac{\mathrm{d}T_{sc}(R_s)}{\mathrm{d}r} = -k_c T_0 \sum_{j=2}^{n} j\tau_j R_s^{j-1}. \tag{C.5}$$

In V_{sc}, we again use the steady-flux solution of the conduction equation (Knibbe and Van Hoolst, 2021)

$$T_{sc}(r) = -\frac{S_{sc}}{6k_c}r^2 + \frac{A_{sc}}{r} + B_{sc}. \tag{C.6}$$

The variables in Eq. (C.6) are given by

$$S_{sc} = -\frac{4\pi\left(q_c R_c^2 - q_s R_s^2\right)}{\frac{4\pi}{3}\left(R_c^3 - R_s^3\right)}, \tag{C.7}$$

$$A_{sc} = \frac{q_c R_c^2}{k_c} - \frac{S_{sc} R_c^3}{3k_c}, \tag{C.8}$$

and

$$B_{sc} = T_s - \frac{A_{sc}}{R_s} + \frac{S_{sc} R_s^2}{6k_c}. \tag{C.9}$$

The thermal energy that corresponds to T_{sc} is

$$\mathscr{E}_{sc} = \rho_c c_c \left(B_{sc} \frac{4\pi}{3}\left(R_c^3 - R_s^3\right) + A_{sc} 2\pi\left(R_c^2 - R_s^2\right) - S_{sc} \frac{4\pi}{30k_c}\left(R_c^5 - R_s^5\right) \right). \tag{C.10}$$

The heat production in V_{ic}, V_{ac}, and V_{sc} become

$$Q_{ic} = \frac{4\pi}{3} R_i^3 \rho_c H_c, \tag{C.11}$$

$$Q_{ac} = Q_{G,ac} + Q_L + \frac{4\pi}{3}\left(R_s^3 - R_i^3\right)\rho_c H_c, \tag{C.12}$$

and

$$Q_{sc} = Q_{G,cc} + \frac{4\pi}{3}\left(R_c^3 - R_s^3\right)\rho_c H_c, \tag{C.13}$$

where H_c is the radiogenic heat production in the core per unit of mass.

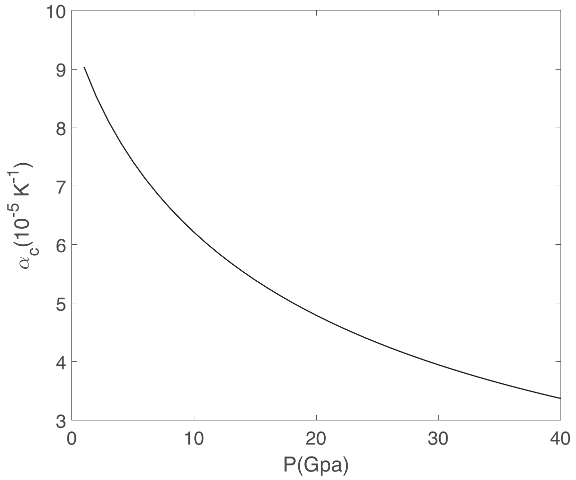

Fig. C.10. Thermal expansion of Fe-7wt%Si-1wt%S-1wt%C of the FESIC model of Knibbe et al. (2021) as a function of pressure, evaluated at 2000 K.

Appendix D. Entropy balance of the core

The core's entropy balance is obtained by integrating the local entropy equation over the core. Neglecting diffusive transport of light elements, as we have done in the thermal evolution model because compositional diffusivity is small, the local entropy equation is (Landau and Lifshitz, 1987; Lister and Buffett, 1995; Gubbins et al., 2004)

$$\rho_c \frac{\mathrm{d}s}{\mathrm{d}t} = \frac{\nabla \cdot k_c \nabla T}{T} + \frac{\rho_c H_c}{T} + \frac{\phi}{T}, \tag{D.1}$$

with s local entropy, $\nabla \cdot k_c T$ dissipation by conduction and ϕ dissipation by viscous and ohmic friction. We note that ohmic friction is commonly assumed to dominate in a low-viscosity liquid planetary core (Lister and Buffett, 1995; Gubbins et al., 2004). Using the thermodynamic identity and definitions of heat capacity and thermal expansion, the left hand side of Eq. (D.1) can be expanded as

$$T\rho_c \frac{\mathrm{d}s}{\mathrm{d}t} = \rho_c c_c \frac{\mathrm{d}T}{\mathrm{d}t} - \rho_c T \frac{\mathrm{d}\mu}{\mathrm{d}t}_{P,X} \frac{\mathrm{d}X}{\mathrm{d}t} - T\alpha_c \frac{\mathrm{d}P}{\mathrm{d}t}, \tag{D.2}$$

where $T(\mathrm{d}\mu/\mathrm{d}t)_{P,X}$, with μ the chemical potential, is the heat of reaction, and the right-most term describes pressure-heating. Because heat of reaction and pressure heating have a minor contribution to the heat and entropy production of the core (Lister and Buffett, 1995; Gubbins et al., 2004; Nimmo, 2007), we have neglected these in our thermal evolution model and the two right-most terms are zero for the thermal evolution scenarios of this paper. A conductive temperature profile has been adopted in the thermally stratified region in the liquid core and in the inner core, such that

$$\rho_c c_c \frac{\mathrm{d}T}{\mathrm{d}t} = \nabla \cdot k_c \nabla T + \rho_c H_c + \phi_X, \tag{D.3}$$

where ϕ_X is ohmic dissipation of work done by F_X which is absent in the inner core. Substitution into Eq. (D.1) shows that the entropy production in the inner core vanishes ($E_{ic} = 0$) and that entropy is in the thermally stratified region of the liquid core exclusively produced by the transport of light elements

$$E_{sc} = \int_{V_{sc}} \frac{F_X}{T}\,\mathrm{d}V. \tag{D.4}$$

To estimate the entropy production in the thermally convective region, we integrate Eq. (D.1)

$$\int_{V_{ac}} \rho_c \frac{\mathrm{d}s}{\mathrm{d}t}\,\mathrm{d}V = \int_{V_{ac}} \frac{\nabla \cdot k_c \nabla T}{T}\,\mathrm{d}V + \int_{V_{ac}} \frac{\rho_c H_c}{T}\,\mathrm{d}V + \int_{V_{ac}} \frac{\phi}{T}\,\mathrm{d}V. \tag{D.5}$$

This first term on the right-hand side can be manipulated using the divergence theorem

$$\int_{V_{ac}} \frac{\nabla \cdot k_c \nabla T}{T}\,\mathrm{d}V = \frac{Q_i}{T_i} - \frac{Q_s}{T_s} + \int_{V_{ac}} k_c \frac{(\nabla T)^2}{T^2}\,\mathrm{d}V. \tag{D.6}$$

By rearranging terms and expanding Q_s in terms of all the internal sources of heat, we obtain

$$\begin{aligned} \int_{V_{ac}} \frac{\phi}{T}\,\mathrm{d}V = {} & \int_{V_{ac}} \left(\frac{1}{T_s} - \frac{1}{T}\right)\left(\rho_c H_c - \rho_c c_c \frac{\mathrm{d}T}{\mathrm{d}t}\right)\mathrm{d}V \\ & + \left(\frac{1}{T_s} - \frac{1}{T_i}\right)(Q_L + Q_i) + \frac{Q_s}{T_s} - \int_{V_{ac}} k_c \frac{(\nabla T)^2}{T^2}\,\mathrm{d}V. \end{aligned} \tag{D.7}$$

This equation can be abbreviated as $E_{ac} = E_H + E_S + E_L + E_i + E_{G,ac} - E_k$ and similar forms of this equation have been given in other literature (Labrosse, 2015; Lister and Buffett, 1995). We remark that we use T_s instead of T_c in these expressions and that the integrals are over V_{ac}, whereas other studies commonly perform the integral over the entire liquid core. But these expressions are, in fact, equivalent, as can be shown from applying the divergence theorem on the expression of E_k for V_{sc}, and using that the temperature profile satisfies the conduction equation. This equation is also equivalent to that of Lister (2003), aside from a term that describes ohmic dissipation in the inner core. Eq. (D.7) is slightly different from that used in Nimmo (2007); Williams et al. (2007); Greenwood et al. (2021a), in which the term Q_i/T_i is not present and the integrals include the inner core. By implementing an adiabat in the thermally stratified inner core, their procedures implicitly assume a downward convective heat flux through the inner core and the adopted entropy balance counts for the corresponding entropy consumption in the inner core.

Finally, we remark that E_{sc} is already in the form of Eq. (41) of the main paper and that E_H, E_S, E_L, E_i, $E_{G,ac}$, and E_k can be written as

$$E_L = Q_L\left(\frac{1}{T_s} - \frac{1}{T_i}\right) = \int_{V_{ac}} \frac{-\frac{\nabla T}{T} q_L}{T}\,\mathrm{d}V, \tag{D.8}$$

with

$$q_L(r) = \frac{Q_L}{4\pi r^2}, \tag{D.9}$$

$$E_{G_{ac}} = \frac{Q_{G_{ac}}}{T_s} = \int_{V_{ac}} \frac{F_X}{T} + \frac{-\frac{\nabla T}{T} q_G}{T}\,\mathrm{d}V, \tag{D.10}$$

with

$$q_G(r) = \int_{R_i}^{r} 4\pi x^2 \phi_G \mathrm{d}x, \tag{D.11}$$

$$E_H = \int_{V_{ac}} \left(\frac{1}{T_s} - \frac{1}{T}\right) \rho_c H_c\,\mathrm{d}V = \int_{V_{ac}} \frac{-\frac{\nabla T}{T} q_H}{T}\,\mathrm{d}V, \tag{D.12}$$

with

$$q_H(r) = \rho_c H_c \frac{4\pi}{3}\left(r^3 - R_i^3\right), \tag{D.13}$$

$$E_S = \int_{V_{ac}} -\left(\frac{1}{T_s} - \frac{1}{T}\right) \rho_c c_c \frac{\mathrm{d}T}{\mathrm{d}t}\,\mathrm{d}V = \int_{V_{ac}} \frac{-\frac{\nabla T}{T} q_S}{T}\,\mathrm{d}V, \tag{D.14}$$

with

$$q_S(r) = \int_{R_i}^{r} -4\pi x^2 \rho_c c_c \frac{\mathrm{d}T}{\mathrm{d}t} \mathrm{d}x, \tag{D.15}$$

$$E_i = 4\pi R_i^2 q_i \left(\frac{1}{T_s} - \frac{1}{T_i}\right) = \int_{V_{ac}} \frac{-\frac{\nabla T}{T} q_i}{T}\,\mathrm{d}V, \tag{D.16}$$

with

$$q_I(r) = \frac{q_i 4\pi R_i^2}{4\pi r^2}, \tag{D.17}$$

and

$$E_k = \int_{V_{ac}} k_c \frac{(\nabla T)^2}{T^2}\,\mathrm{d}V = \int_{V_{ac}} \frac{-\frac{\nabla T}{T} q_k}{T}\,\mathrm{d}V. \tag{D.18}$$

with

$$q_k(r) = -k_c \nabla T. \tag{D.19}$$

We can now write the entropy balance as $E_\Phi = E_L + E_{G,ac} + E_{G,sc} + E_H + E_S + E_i - E_k$. Using $q_T^* = q_T - q_k$, with $q_T = q_L + q_G + q_H + q_S + q_I$ and realising that $F_X = 0$ in the (assumed compositionally stratified and not convective) inner core and $F_T = 0$ in the thermally stratified region of the liquid core, we obtain Eq. (41) of the main paper.

Data availability

The code that is developed for this study and used to produce the results in this paper is freely available at an online repository (Knibbe, 2024).

References

Anderson, B.J., Johnson, C.L., Korth, H., Winslow, R.M., Borovsky, J.E., Purucker, M.E., Slavin, J.A., Solomon, S.C., Zuber, M.T., McNutt Jr., R.L., 2012. Low-degree structure in Mercury's planetary magnetic field. J. Geophys. Res. Planets 117. https://doi.org/10.1029/2012JE004159.

Berrada, M., Secco, R.A., Yong, W., 2021. Adiabatic heat flow in Mercury's core from electrical resistivity measurements of liquid Fe-8.5 wt%Si to 24 GPa. Earth Planet. Sci. Lett. 568, 117053. URL: https://www.sciencedirect.com/science/article/pii/S0012821X21003083 https://doi.org/10.1016/j.epsl.2021.117053.

Boujibar, A., Habermann, M., Righter, K., Ross, D.K., Pando, K., Righter, M., Chidester, B. A., Danielson, L.R., 2019. U, Th, and K partitioning between metal, silicate, and sulfide and implications for Mercury's structure, volatile content, and radioactive heat production. Am. Mineral. 104, 1221–1237. https://doi.org/10.2138/am-2019-7000.

Breuer, D., 2011. Stagnant Lid Convection. Springer Berlin Heidelberg, Berlin, Heidelberg, p. 1569. https://doi.org/10.1007/978-3-642-11274-4_1499.

Buffet, B., 2014. Geomagnetic fluctuations reveal stable stratification at the top of the Earth's core. Nature 507, 484–487. https://doi.org/10.1038/nature13122.

Buffett, B., 2012. Geomagnetism under scrutiny. Nature 485, 319–320. https://doi.org/10.1038/485319a.

Chabot, N.L., Wollack, E.A., Klima, R.L., Minitti, M.E., 2014. Experimental constraints on Mercury's core composition. Earth Planet. Sci. Lett. 390, 199–208. https://doi.org/10.1016/j.epsl.2014.01.004.

Chen, B., Li, J., Hauck II, S.A., 2008. Non-ideal liquidus curve in the Fe-S system and Mercury's snowing core. Geophys. Res. Lett. 35. https://doi.org/10.1029/2008GL033311.

Christensen, U.R., 2006. A deep dynamo generating Mercury's magnetic field. Nature 444, 1056–1058. https://doi.org/10.1038/nature05342.

Christensen, U.R., Wicht, J., 2008. Models of magnetic field generation in partly stable planetary cores: applications to Mercury and Saturn. Icarus 196, 16–34. https://doi.org/10.1016/j.icarus.2008.02.013.

Davaille, A., Jaupart, C., 1993. Transient high-Rayleigh-number thermal convection with large viscosity variations. J. Fluid Mech. 253, 141–166. https://doi.org/10.1017/S0022112093001740.

Davies, C.J., 2015. Cooling history of Earth's core with high thermal conductivity. Phys. Earth Planet. Inter. 247, 65–79. https://doi.org/10.1016/j.pepi.2015.03.007.

Davies, C.J., Pommier, A., Greenwood, S., Wilson, A., 2024. Thermal and magnetic evolution of Mercury with a layered Fe-Si(-S) core. Earth Planet. Sci. Lett. 641, 118812. https://doi.org/10.1016/j.epsl.2024.118812.

de Koker, N., Steinle-Neumann, G., Vlček, V., 2012. Electrical resistivity and thermal conductivity of liquid Fe alloys at high P and T, and heat flux in Earth’s core. Proc. Natl. Acad. Sci. 109, 4070–4073. https://doi.org/10.1073/pnas.1111841109.

Denevi, B.W., Ernst, C.M., Meyer, H.M., Robinson, M.S., Murchie, S.L., Whitten, J.L., Head, J.W., Watters, T.R., Solomon, S.C., Ostrach, L.R., Chapman, C.R., Byrne, P.K., Klimczak, C., Peplowski, P.N., 2013. The distribution and origin of smooth plains on Mercury. J. Geophys. Res. Planets 118, 891–907. https://doi.org/10.1002/jgre.20075.

Deng, L., Fei, Y., Liu, X., Gong, Z., Shahar, A., 2013. Effect of carbon, sulfur and silicon on iron melting at high pressure: implications for composition and evolution of the planetary terrestrial cores. Geochim. Cosmochim. Acta 114, 220–233. URL. https://www.sciencedirect.com/science/article/pii/S0016703713000458. https://doi.org/10.1016/j.gca.2013.01.023.

Desai, P.D., 1985. Thermodynamic properties of iron and silicon. J. Phys. Chem. Ref. Data Monogr. 15. https://doi.org/10.1063/1.555761.

Dumberry, M., Rivoldini, A., 2015. Mercury's inner core size and core-crystallization regime. Icarus 248, 254–268. https://doi.org/10.1016/j.icarus.2014.10.038.

Edmund, E., Morard, G., Baron, M.A., Rivoldini, A., Yokoo, S., Boccato, S., Hirose, K., Pakhomova, A., Antonangeli, D., 2022. The Fe-FeSi phase diagram at Mercury's core conditions. Nat. Commun. 13, 387. https://doi.org/10.1038/s41467-022-27991-9.

Fei, Y., Brosh, E., 2014. Experimental study and thermodynamic calculations of phase relations in the Fe–C system at high pressure. Earth Planet. Sci. Lett. 408, 155–162. https://doi.org/10.1016/j.epsl.2014.09.044.

Fei, Y., Bertka, C.M., Finger, L.W., 1997. High-pressure iron-sulfur compound, Fe3S2, and melting relations in the Fe-FeS system. Science 275, 1621–1623. https://doi.org/10.1126/science.275.5306.1621.

Fei, Y., Li, J., Bertka, C.M., Prewitt, C.T., 2000. Structure type and bulk modulus of Fe3S, a new iron-sulfur compound. Am. Mineral. 85, 1830–1833. https://doi.org/10.2138/am-2000-11-1229.

Fleury, A., Plesa, A.-C., Hüttig, C., Breuer, D., 2024. Assessing the Accuracy of 2-D Planetary Evolution Models Against the 3-D Sphere. Geochem. Geophy. Geosys. 25 (2), e2023GC011114. https://doi.org/10.1029/2023GC011114.

Freitas, D., Monteux, J., Andrault, D., Manthilake, G., Mathieu, A., Schiavi, F., Cluzel, N., 2021. Thermal conductivities of solid and molten silicates: implications for dynamos in mercury-like proto-planets. Phys. Earth Planet. Inter. 312, 106655. URL. https://www.sciencedirect.com/science/article/pii/S0031920121000133. https://doi.org/10.1016/j.pepi.2021.106655.

Garaud, P., 2018. Double-diffusive convection at low Prandtl number. Annu. Rev. Fluid Mech. 50, 275–298. https://doi.org/10.1146/annurev-fluid-122316-045234.

Garaud, P., 2020. Double-Diffusive Processes in Stellar Astrophysics. EDP Sciences, Les Ulis, pp. 13–60. https://doi.org/10.1051/978-2-7598-2437-3.c003.

Genova, A., Hussmann, H., Van Hoolst, T., Heyner, D., Iess, L., Santoli, F., Thomas, N., Cappuccio, P., di Stefano, I., Kolhey, P., Langlais, B., Mieth, J.Z.D., Oliveira, J.S., Stark, A., Steinbrügge, G., Tosi, N., Wicht, J., Benkhoff, J., 2021. Geodesy, geophysics and fundamental physics investigations of the BepiColombo mission. Space Sci. Rev. 217, 31. https://doi.org/10.1007/s11214-021-00808-9.

Grasset, O., Parmentier, E.M., 1998. Thermal convection in a volumetrically heated, infinite Prandtl number fluid with strongly temperature-dependent viscosity: implications for planetary thermal evolution. J. Geophys. Res. Solid Earth 103, 18171–18181. https://doi.org/10.1029/98JB01492.

Greenwood, S., Davies, C.J., Mound, J.E., 2021a. On the evolution of thermally stratified layers at the top of Earth's core. Phys. Earth Planet. Inter. 318, 106763. https://doi.org/10.1016/j.pepi.2021.106763.

Greenwood, S., Davies, C.J., Pommier, A., 2021b. Influence of thermal stratification on the structure and evolution of the Martian core. Geophys. Res. Lett. 48, e2021GL095198. https://doi.org/10.1029/2021GL095198.

Grott, M., Breuer, D., Laneuville, M., 2011. Thermo-chemical evolution and global contraction of Mercury. Earth Planet. Sci. Lett. 307, 135–146. https://doi.org/10.1016/j.epsl.2011.04.040.

Gubbins, D., Alfè, D., Masters, G., Price, G.D., Gillan, M.J., 2003. Can the Earth's dynamo run on heat alone? Geophys. J. Int. 155, 609–622. https://doi.org/10.1046/j.1365-246X.2003.02064.x.

Gubbins, D., Alfè, D., Masters, G., Price, G.D., Gillan, M., 2004. Gross thermodynamics of two-component core convection. Geophys. J. Int. 157, 1407–1414. https://doi.org/10.1111/j.1365-246X.2004.02219.x.

Gubbins, D., Alfè, D., Davies, C.J., 2013. Compositional instability of Earth's solid inner core. Geophys. Res. Lett. 40, 1084–1088. https://doi.org/10.1002/grl.50186.

Guerrero, J., Lowman, J., Tackley, P., 2021. Did the cessation of convection in Mercury's mantle allow for a dynamo supporting increase in heat loss from its core? Earth Planet. Sci. Lett. 571, 117108. https://doi.org/10.1016/j.epsl.2021.117108.

Guervilly, C., 2022. Fingering convection in the stably stratified layers of planetary cores. J. Geophys. Res. Planets 127, e2022JE007350. https://doi.org/10.1029/2022JE007350.

Hauck, S.A., Dombard, A.J., Phillips, R.J., Solomon, S.C., 2004. Internal and tectonic evolution of Mercury. Earth Planet. Sci. Lett. 222, 713–728. https://doi.org/10.1016/j.epsl.2004.03.037.

Hüttig, C., Tosi, N., Moore, W.B., 2013. An improved formulation of the incompressible Navier–Stokes equations with variable viscosity. Phys. Earth Planet. Inter. 220, 11–18. URL. https://www.sciencedirect.com/science/article/pii/S0031920113000459. https://doi.org/10.1016/j.pepi.2013.04.002.

Johnson, C.L., Phillips, R.J., Purucker, M.E., Anderson, B.J., Byrne, P.K., Denevi, B.W., Feinberg, J.M., Hauck, S.A., Head, J.W., Korth, H., James, P.B., Mazarico, E., Neumann, G.A., Philpott, L.C., Siegler, M.A., Tsyganenko, N.A., Solomon, S.C., 2015. Low-altitude magnetic field measurements by MESSENGER reveal Mercury's ancient crustal field. Science 348, 892–895. URL. https://www.science.org/doi/abs/10.1126/science.aaa8720. https://doi.org/10.1126/science.aaa8720.

Knibbe, J., 2024. Code for modelling the thermal evolution and dynamo evolution of planet Mercury. URL. https://doi.org/10.5281/zenodo.14019151.

Knibbe, J., Van Hoolst, T., 2021. Modelling of thermal stratification at the top of a planetary core: application to the cores of Earth and Mercury and the thermal coupling with their mantles. Phys. Earth Planet. Inter. 321, 106804. https://doi.org/10.1016/j.pepi.2021.106804.

Knibbe, J.S., van Westrenen, W., 2015. The interior configuration of planet Mercury constrained by moment of inertia and planetary contraction. J. Geophys. Res. Planets 120, 1904–1923. https://doi.org/10.1002/2015JE004908.

Knibbe, J.S., van Westrenen, W., 2018. The thermal evolution of Mercury's Fe–Si core. Earth Planet. Sci. Lett. 482, 147–159. https://doi.org/10.1016/j.epsl.2017.11.006.

Knibbe, J.S., Rivoldini, A., Luginbuhl, S.M., Namur, O., Charlier, B., Mezouar, M., Sifre, D., Berndt, J., Kono, Y., Neuville, D.R., van Westrenen, W., Van Hoolst, T., 2021. Mercury's interior structure constrained by density and p-wave velocity measurements of liquid Fe-Si-C alloys. J. Geophys. Res. Planets 126, e2020JE006651. https://doi.org/10.1029/2020JE006651. e2020JE006651 2020JE006651.

Konrad, W., Spohn, T., 1997. Thermal history of the Moon: implications for an early core dynamo and post-accertional magmatism. Adv. Space Res. 19, 1511–1521. https://doi.org/10.1016/S0273-1177(97)00364-5. proceedings of the BO.1 Symposium of COSPAR Scientific Commission B.

Kunze, E., 2003. A review of oceanic salt-fingering theory. Prog. Oceanogr. 56, 399–417. https://doi.org/10.1016/S0079-6611(03)00027-2. double-Diffusion in Oceanography.

Labrosse, S., 2014. Thermal and compositional stratification of the inner core. Compt. Rendus Geosci. 346, 119–129. https://doi.org/10.1016/j.crte.2014.04.005. earth's inner core.

Labrosse, S., 2015. Thermal evolution of the core with a high thermal conductivity. Phys. Earth Planet. Inter. 247, 36–55. https://doi.org/10.1016/j.pepi.2015.02.002. transport Properties of the Earth's Core.

Labrosse, S., Poirier, J.P., Le Mouël, J.L., 1997. On cooling of the Earth's core. Phys. Earth Planet. Inter. 99, 1–17. https://doi.org/10.1016/S0031-9201(96)03207-4.

Landau, L., Lifshitz, E., 1987. Chapter VI - Diffusion. In: Landau, L.D., Lifshitz, E.M. (Eds.), Fluid Mechanics (Second Edition), second edition ed. Pergamon, pp. 227–237. URL. https://www.sciencedirect.com/science/article/pii/B9780080339337500143. https://doi.org/10.1016/B978-0-08-033933-7.50014-3.

Lapwood, E.R., 1952. The effect of contraction in the cooling by conduction of a gravitating sphere, with special reference to the Earth. Geophys. J. Int. 6, 402–407. https://doi.org/10.1111/j.1365-246X.1952.tb03027.x.

Lister, J.R., 2003. Expressions for the dissipation driven by convection in the Earth's core. Phys. Earth Planet. Inter. 140, 145–158. https://doi.org/10.1016/j.pepi.2003.07.007.

Lister, J.R., Buffett, B.A., 1995. The strength and efficiency of thermal and compositional convection in the geodynamo. Phys. Earth Planet. Inter. 91, 17–30. https://doi.org/10.1016/0031-9201(95)03042-U.

Lister, J.R., Buffett, B.A., 1998. Stratification of the outer core at the core-mantle boundary. Phys. Earth Planet. Inter. 105, 5–19. URL: https://www.sciencedirect.com/science/article/pii/S0031920197000824 https://doi.org/10.1016/S0031-9201(97)00082-4.

Loper, D.E., 1978. Some thermal consequences of a gravitationally powered dynamo. J. Geophys. Res. Solid Earth 83, 5961–5970. https://doi.org/10.1029/JB083iB12p05961.

Maaløe, S., 2004. The solidus of harzburgite to 3 GPa pressure: the compositions of primary abyssal tholeiite. Mineral. Petrol. 81, 1–17. https://doi.org/10.1007/s00710-004-0028-6.

Manglik, A., Wicht, J., Christensen, U.R., 2010. A dynamo model with double diffusive convection for Mercury's core. Earth Planet. Sci. Lett. 289, 619–628. https://doi.org/10.1016/j.epsl.2009.12.007.

Marchi, S., Chapman, C.R., Fassett, C.I., Head, J.W., Bottke, W.F., Strom, R.G., 2013. Global resurfacing of Mercury 4.0–4.1 billion years ago by heavy bombardment and volcanism. Nature 499, 59–61. https://doi.org/10.1038/nature12280.

Michel, N.C., Hauck II, S.A., Solomon, S.C., Phillips, R.J., Roberts, J.H., Zuber, M.T., 2013. Thermal evolution of Mercury as constrained by MESSENGER observations. J. Geophys. Res. Planets 118, 1033–1044. https://doi.org/10.1002/jgre.20049.

Morard, G., Andrault, D., Guignot, N., Siebert, J., Garbarino, G., Antonangeli, D., 2011. Melting of Fe–Ni–Si and Fe–Ni–S alloys at megabar pressures: implications for the core–mantle boundary temperature. Phys. Chem. Miner. 38, 767–776. https://doi.org/10.1007/s00269-011-0449-9.

Morard, G., Siebert, J., Badro, J., 2014. Partitioning of Si and platinum group elements between liquid and solid Fe–Si alloys. Geochim. Cosmochim. Acta 132, 94–100. URL. https://www.sciencedirect.com/science/article/pii/S001670371400088X. https://doi.org/10.1016/j.gca.2014.01.044.

Morard, G., Boccato, S., Rosa, A.D., Anzellini, S., Miozzi, F., Henry, L., Garbarino, G., Mezouar, M., Harmand, M., Guyot, F., Boulard, E., Kantor, I., Irifune, T., Torchio, R., 2018. Solving controversies on the iron phase diagram under high pressure. Geophys. Res. Lett. 45, 11,074–11,082. https://doi.org/10.1029/2018GL079950.

Morschhauser, A., Grott, M., Breuer, D., 2011. Crustal recycling, mantle dehydration, and the thermal evolution of Mars. Icarus 212, 541–558. https://doi.org/10.1016/j.icarus.2010.12.028.

Namur, O., Charlier, B., Holtz, F., Cartier, C., McCammon, C., 2016a. Sulfur solubility in reduced mafic silicate melts: implications for the speciation and distribution of sulfur on Mercury. Earth Planet. Sci. Lett. 448, 102–114. https://doi.org/10.1016/j.epsl.2016.05.024.

Namur, O., Collinet, M., Charlier, B., Grove, T.L., Holtz, F., McCammon, C., 2016b. Melting processes and mantle sources of lavas on Mercury. Earth Planet. Sci. Lett. 439, 117–128. URL. https://www.sciencedirect.com/science/article/pii/S0012821X16000522. https://doi.org/10.1016/j.epsl.2016.01.030.

Nimmo, F., 2007. 8.02 - Energetics of the core. In: Schubert, G. (Ed.), Treatise on Geophysics. Elsevier, Amsterdam, pp. 31–65. https://doi.org/10.1016/B978-044452748-6.00128-0.

Nishi, T., Shibata, H., Waseda, Y., Ohta, H., 2003. Thermal conductivities of molten iron, cobalt, and nickel by laser flash method. Metall. Mater. Trans. A 34, 2801–2807. https://doi.org/10.1007/s11661-003-0181-2.

Ozawa, H., Hirose, K., Yonemitsu, K., Ohishi, Y., 2016. High-pressure melting experiments on Fe–Si alloys and implications for silicon as a light element in the core. Earth Planet. Sci. Lett. 456, 47–54. https://doi.org/10.1016/j.epsl.2016.08.042.

Padovan, S., Wieczorek, M.A., Margot, J.L., Tosi, N., Solomon, S.C., 2015. Thickness of the crust of Mercury from geoid-to-topography ratios. Geophys. Res. Lett. 42, 1029–1038. https://doi.org/10.1002/2014GL062487.

Pease, A., Li, J., 2022. Liquidus determination of the Fe-S and (Fe, Ni)-S systems at 14 and 24 GPa: implications for the Mercurian core. Earth Planet. Sci. Lett. 599, 117865. URL. https://www.sciencedirect.com/science/article/pii/S0012821X22005015. https://doi.org/10.1016/j.epsl.2022.117865.

Peplowski, P.N., Evans, L.G., Hauck, S.A., McCoy, T.J., Boynton, W.V., Gillis-Davis, J.J., Ebel, D.S., Goldsten, J.O., Hamara, D.K., Lawrence, D.J., McNutt, R.L., Nittler, L.R., Solomon, S.C., Rhodes, E.A., Sprague, A.L., Starr, R.D., Stockstill-Cahill, K.R., 2011. Radioactive elements on Mercury's surface from MESSENGER: implications for the planet's formation and evolution. Science 333, 1850–1852. https://doi.org/10.1126/science.1211576.

Radko, T., 2013. Double-Diffusive Convection. Cambridge University Press. https://doi.org/10.1017/CBO9781139034173.

Sakai, F., Hirose, K., Morard, G., 2023. Partitioning of silicon and sulfur between solid and liquid iron under core pressures: constraints on Earth's core composition. Earth Planet. Sci. Lett. 624, 118449. URL: https://www.sciencedirect.com/science/article/pii/S0012821X23004624 https://doi.org/10.1016/j.epsl.2023.118449.

Scheil, E., 1942. Bemerkungen zur schichtkristallbildung. Int. J. Mater. Res. 34, 70–72.

Schmitt, R.W., 1983. The characteristics of salt fingers in a variety of fluid systems, including stellar interiors, liquid metals, oceans, and magmas. Phys. Fluids 26, 2373–2377. https://doi.org/10.1063/1.864419.

Schubert, G., Cassen, P., Young, R., 1979. Subsolidus convective cooling histories of terrestrial planets. Icarus 38, 192–211. https://doi.org/10.1016/0019-1035(79)90178-7.

Schubert, G., Turcotte, D.L., Olson, P., 2001. Mantle Convection in the Earth and Planets. Cambridge University Press.

Secco, R.A., 2017. Thermal conductivity and Seebeck coefficient of Fe and Fe-Si alloys: implications for variable Lorenz number. Phys. Earth Planet. Inter. 265, 23–34. URL. https://www.sciencedirect.com/science/article/pii/S0031920116301832. https://doi.org/10.1016/j.pepi.2017.01.005.

Steenstra, E., van Westrenen, W., 2020. Geochemical constraints on core-mantle differentiation in Mercury and the aubrite parent body. Icarus 340, 113621. URL. https://www.sciencedirect.com/science/article/pii/S0019103519303902. https://doi.org/10.1016/j.icarus.2020.113621.

Stern, M.E., 1960. The "salt-fountain" and thermohaline convection. Tellus 12, 172–175. https://doi.org/10.3402/tellusa.v12i2.9378.

Stevenson, D.J., Spohn, T., Schubert, G., 1983. Magnetism and thermal evolution of the terrestrial planets. Icarus 54, 466–489. https://doi.org/10.1016/0019-1035(83)90241-5.

Takahashi, F., Shimizu, H., Tsunakawa, H., 2019. Mercury's anomalous magnetic field caused by a symmetry-breaking self-regulating dynamo. Nat. Commun. 10, 208. https://doi.org/10.1038/s41467-018-08213-7.

Tao, R., Fei, Y., 2021. High-pressure experimental constraints of partitioning behavior of Si and S at the Mercury's inner core boundary. Earth Planet. Sci. Lett. 562, 116849. URL: https://www.sciencedirect.com/science/article/pii/S0012821X21001084 https://doi.org/10.1016/j.epsl.2021.116849.

Terasaki, H., Rivoldini, A., Shimoyama, Y., Nishida, K., Urakawa, S., Maki, M., Kurokawa, F., Takubo, Y., Shibazaki, Y., Sakamaki, T., Machida, A., Higo, Y., Uesugi, K., Takeuchi, A., Watanuki, T., Kondo, T., 2019. Pressure and composition effects on sound velocity and density of core-forming liquids: implication to core compositions of terrestrial planets. J. Geophys. Res. Planets 124, 2272–2293. https://doi.org/10.1029/2019JE005936.

Thébault, E., Langlais, B., Oliveira, J., Amit, H., Leclercq, L., 2018. A time-averaged regional model of the Hermean magnetic field. Phys. Earth Planet. Inter. 276, 93–105. URL. https://www.sciencedirect.com/science/article/pii/S0031920117300304. https://doi.org/10.1016/j.pepi.2017.07.001 (special Issue:15th SEDI conference).

Thiriet, M., Breuer, D., Michaut, C., Plesa, A.C., 2019. Scaling laws of convection for cooling planets in a stagnant lid regime. Phys. Earth Planet. Inter. 286, 138–153. https://doi.org/10.1016/j.pepi.2018.11.003.

Tosi, N., Grott, M., Plesa, A.C., Breuer, D., 2013a. Thermochemical evolution of Mercury's interior. J. Geophys. Res. Planets 118, 2474–2487. https://doi.org/10.1002/jgre.20168.

Tosi, N., Yuen, D.A., de Koker, N., Wentzcovitch, R.M., 2013b. Mantle dynamics with pressure- and temperature-dependent thermal expansivity and conductivity. Phys. Earth Planet. Inter. 217, 48–58. URL. https://www.sciencedirect.com/science/article/pii/S0031920113000289. https://doi.org/10.1016/j.pepi.2013.02.004.

Vander Kaaden, K.E., McCubbin, F.M., Turner, A.A., Ross, D.K., 2020. Constraints on the abundances of carbon and silicon in Mercury's core from experiments in the Fe-Si-C system. J. Geophys. Res. Planets 125, e2019JE006239. https://doi.org/10.1029/2019JE006239.

Wardinski, I., Langlais, B., Thébault, E., 2019. Correlated time-varying magnetic fields and the core size of Mercury. J. Geophys. Res. (Planets) 124, 2178–2197. https://doi.org/10.1029/2018JE005835.

Wardinski, I., Amit, H., Langlais, B., Thébault, E., 2021. The internal structure of Mercury's core inferred from magnetic observations. J. Geophys. Res. Planets 126.

Williams, J.P., Aharonson, O., Nimmo, F., 2007. Powering Mercury's dynamo. Geophys. Res. Lett. 34. https://doi.org/10.1029/2007GL031164.

Zhang, Y., Yoshino, T., Yoneda, A., Osako, M., 2019. Effect of iron content on thermal conductivity of olivine with implications for cooling history of rocky planets. Earth Planet. Sci. Lett. 519, 109–119. URL: https://www.sciencedirect.com/science/article/pii/S0012821X19302602 https://doi.org/10.1016/j.epsl.2019.04.048.

Zhang, Y., Luo, K., Hou, M., Driscoll, P., Salke, N.P., Minár, J., Prakapenka, V.B., Greenberg, E., Hemley, R.J., Cohen, R.E., Lin, J.F., 2022. Thermal conductivity of Fe-Si alloys and thermal stratification in Earth's core. Proc. Natl. Acad. Sci. 119, e2119001119. https://doi.org/10.1073/pnas.2119001119.

Zolotov, M.Y., Sprague, A.L., Hauck, S.A., Nittler, L.R., Solomon, S.C., Weider, S.Z., 2013. The redox state, FeO content, and origin of sulfur-rich magmas on Mercury. J. Geophys. Res. Planets 118, 138–146. https://doi.org/10.1029/2012je004274.